Research Square

Preprints are preliminary reports that have not undergone peer review.
They should not be considered conclusive, used to inform clinical practice,
or referenced by the media as validated information.

The tumor microenvironment landscape in lung adenocarcinoma with spatial transcriptomic mapping

Jiao Nie[1]
Guangzhou University of Chinese Medicine
Wenyuan Song[1]
Guangzhou University of Chinese Medicine
Bowen Yang[1]
Guangzhou University of Chinese Medicine
Xiaotong Li[1]
Guangzhou University of Chinese Medicine
Wenxin Li[1]
Guangzhou University of Chinese Medicine
Panpan Duan[1]
Guangzhou University of Chinese Medicine
Xuejiao Lv[1]
Guangzhou University of Chinese Medicine
Shufang Hou[1]
sfhoudgzyy@163.com

Guangzhou University of Chinese Medicine

Article

Keywords:

Posted Date: September 25th, 2026

DOI: https://doi.org/10.21203/rs.3.rs-10946821/v1

License: This work is licensed under a Creative Commons Attribution 4.0 International License.
Read Full License

Additional Declarations: No competing interests reported.

The tumor microenvironment landscape in lung adenocarcinoma with spatial transcriptomic mapping

Jiao Nie[1], Wenyuan Song[1], Bowen Yang[1], Xiaotong Li[1], Wenxin Li[1], Panpan Duan[1], Xuejiao Lv[1], Shufang Hou[1],✉

[1] Guangzhou University of Chinese Medicine Dongguan Hospital (Dongguan Hospital of Traditional Chinese Medicine)

Jiao Nie: nj764104075@163.com; Wenyuan Song: 820200575@qq.com

Bowen Yang: 867571621@qq.com; Xiaotong Li: 1121997455@qq.com

Wenxin Li: Li_wen_xin@hotmail.com; Panpan Duan: 2670588871@qq.com

Xuejiao Lv: eden980112@163.com

✉ Corresponding author: sfhoudgzyy@163.com

Abstract

Spatial communication in tumor microenvironment remains incompletely defined in lung adenocarcinoma. We integrated 196,301 single cells with 19,039 Visium spots across six samples to map cellular organization and candidate local signaling. The atlas resolved 31 cell types and sample-specific spatial domains. Coupling cell2location with LIANA prioritized 3,451 spatially constrained ligand-receptor interactions. Major signals encompassed tissue remodeling (TIMP1-CD63), adenosine-mediated immunosuppression (ADO-ADORA2B), and stem cell maintenance (LIF-IL6ST/LIFR), supporting a link between epithelial repair, tumor growth, and immune evasion. Spatially informed in silico perturbation nominated proliferating alveolar macrophages and TIMP1-CD63 as high-dependency network components. Plasma-cell autocorrelation supported heterogeneous TLS-like organization. In an independent pretreatment anti-PD-1 NSCLC cohort, T cell exhaustion/checkpoint and TLS/plasma-B-cell signatures were responder-enriched (AUC = 0.91, FDR = 0.033; AUC = 0.85, FDR = 0.094). These analyses nominate recurrent spatial immune states and candidate communication dependencies for functional validation.

Introduction

Lung cancer remains the leading cause of cancer-related mortality worldwide, with non-small cell lung cancer (NSCLC) accounting for approximately 85% of all diagnoses[1]. Targeted therapy and immunotherapy, particularly immune checkpoint inhibitors (ICIs) directed against PD-1/PD-L1 and CTLA-4[2],[3], have transformed treatment paradigms. Yet only 20–30% of patients achieve durable clinical responses[4],[5], emphasizing the need for a deeper mechanistic understanding of the tumor microenvironment (TME) and its role in therapeutic resistance.

The TME constitutes a complex and dynamic ecosystem comprising tumor cells, immune cells, stromal cells, and extracellular matrix components that collectively govern tumor progression and therapeutic outcome[6]. Single-cell RNA sequencing (scRNA-seq) has enabled increasingly resolved analysis of cellular heterogeneity in the TME[7],[8]. Landmark studies have delineated the immune landscape of NSCLC, uncovering extensive phenotypic diversity among T cell, macrophage, and dendritic cell populations[9],[10]. However, these studies provide limited information about the spatial organization of intercellular communication.

Spatial transcriptomics technologies, particularly the 10x Visium platform, have emerged as powerful modalities for preserving tissue architecture while profiling gene expression across intact tissue sections[11],[12]. When coupled with scRNA-seq data through computational deconvolution approaches such as cell2location[13], spatial transcriptomics enables cell type mapping at spot-level resolution. This facilitates identification of spatially constrained cell–cell communication, making the integration particularly valuable for elucidating how physical proximity shapes functional states and signaling patterns in the TME.

Cell–cell communication analysis with frameworks such as LIANA[14] has revealed extensive ligand–receptor signaling networks in tumors. Most existing analysis, however, fails to incorporate spatial constraints and may therefore identify interactions between cell types that do not physically co-localize in intact tissue. Recent investigations in breast cancer[15] and pancreatic cancer[16] have emphasized the importance of spatial context when interpreting local communication programs. NSCLC spatial atlases have characterized cellular ecosystems at the tissue level (Leader et al., 2021)[17] and mapped high-resolution immune landscapes (Salcher et al., 2022)[18]. However, systematic integration of scRNA-seq-derived communication networks with spatial co-localization statistics, supported by permutation testing, remains limited.

Furthermore, the relationship between TME spatial organization and clinical outcomes, particularly response to immunotherapy, remains poorly characterized. Although tertiary lymphoid structures (TLS) have been associated with favorable prognosis and enhanced ICI responsiveness[19],[20], their spatial

relationship with other TME components and their role in modulating local immune responses remain unclear. T cell exhaustion, a principal mechanism of immune evasion, also exhibits spatial heterogeneity that may influence therapeutic outcomes[21],[22].

In this study, we present an integrated analysis of scRNA-seq and spatial transcriptomics data from NSCLC patients, addressing three central questions: (1) How are diverse cell types spatially organized in the TME of NSCLC? (2) Which cell–cell communication networks are spatially constrained and reproducible across samples? (3) How do spatial immune states relate to candidate immunotherapy-relevant biomarkers? Through cell2location deconvolution integrated with LIANA communication analysis, we identify spatially constrained interactions supported by permutation testing and cross-sample recurrence analysis. We map T cell exhaustion, TLS-associated plasma-cell organization, and stage- and tissue-origin-linked TME remodeling, and evaluate immune-state signatures in an independent pretreatment anti-PD-1 cohort to define testable spatial hypotheses for NSCLC TME biology and immunotherapy response.

Results

Comprehensive single-cell atlas identifies 31 distinct cell types in the TME of NSCLC

To construct a broad cellular atlas in the TME of NSCLC, we analyzed 196,301 high-quality cells derived from 58 samples representing seven tissue types (lung tumor, normal lung, tumor lymph node, normal lymph node, metastatic lymph node, pleural effusion, and metastatic brain) across 44 patients (Fig. 1b–c, Supplementary Fig. 1a–d). Following stringent quality control filtering and batch correction with Harmony[23], we then performed Leiden clustering and automated cell type annotation with CellTypist[24]. This process identified 31 distinct cell types containing the immune, epithelial, and stromal compartments (Fig. 1a, Supplementary Table 1).

The immune compartment was dominated by T lymphocytes. $CD4^+$ T cells constituted the largest population (52,643 cells; 26.8%), followed by $CD8^+$ T cells (24,206 cells; 12.3%) and natural killer (NK) cells (12,594 cells; 6.4%), collectively accounting for over 45% of all profiled cells (Fig. 1a,d; Supplementary Table 1). We note that $CD4^+$ and $CD8^+$ T cells were annotated at a coarse granularity; finer sub-clustering into Treg, Th1, Th17, Tfh, and exhaustion states was not performed at this level, but they were partially captured through our downstream exhaustion scoring analysis. This substantial T cell infiltration is consistent with the immunogenic character of NSCLC and provides the cellular substrate for immunotherapy responsiveness. B lymphocytes represented 12.1% of cells (23,659 cells), with a subset differentiating into plasma cells (3,786 cells; 1.9%), indicating the active humoral immune responses.

The myeloid compartment comprised monocyte-derived macrophages (14,384 cells; 7.3%), alveolar macrophages (12,859 cells; 6.5%), classical monocytes (3,604 cells; 1.8%), and multiple dendritic cell (DC) subsets (DC2: 6,002 cells; migratory DCs; plasmacytoid DCs), consistent with the diverse myeloid landscape of NSCLC.

The epithelial compartment was predominantly represented by alveolar type II (AT2) cells (19,758 cells; 10.1%), including a proliferating subpopulation (AT2 proliferating) compatible with ongoing alveolar repair processes. Additional epithelial populations included AT1 cells, Club cells, multiciliated cells, and deuterosomal cells, representing airway and alveolar epithelial lineages. The stromal compartment comprised distinct fibroblast subtypes (adventitial and alveolar fibroblasts), smooth muscle cells, and multiple endothelial cell populations (general capillary, arterial, and venous), reflecting the vascular complexity of the TME.

Differential gene expression analysis identified 26,755 significantly differentially expressed gene entries (FDR < 0.05, $|\log_2 FC| > 1$) across cell types (Supplementary Fig. 1e, Supplementary Data 1). $CD4^+$ T cells had the highest number of differentially expressed genes (1,565 genes), followed by AT2 cells (1,424 genes) and B cells (1,381 genes), reflecting their transcriptional diversity and functional specialization.

Notably, we observed substantial heterogeneity in cell type composition across tissue types (Fig. 1d). Tumor samples were enriched for immunosuppressive myeloid populations and exhausted T cells relative to normal tissues, whereas lymph node samples showed elevated proportions of B cells and plasma cells, consistent with their role as sites of adaptive immune priming.

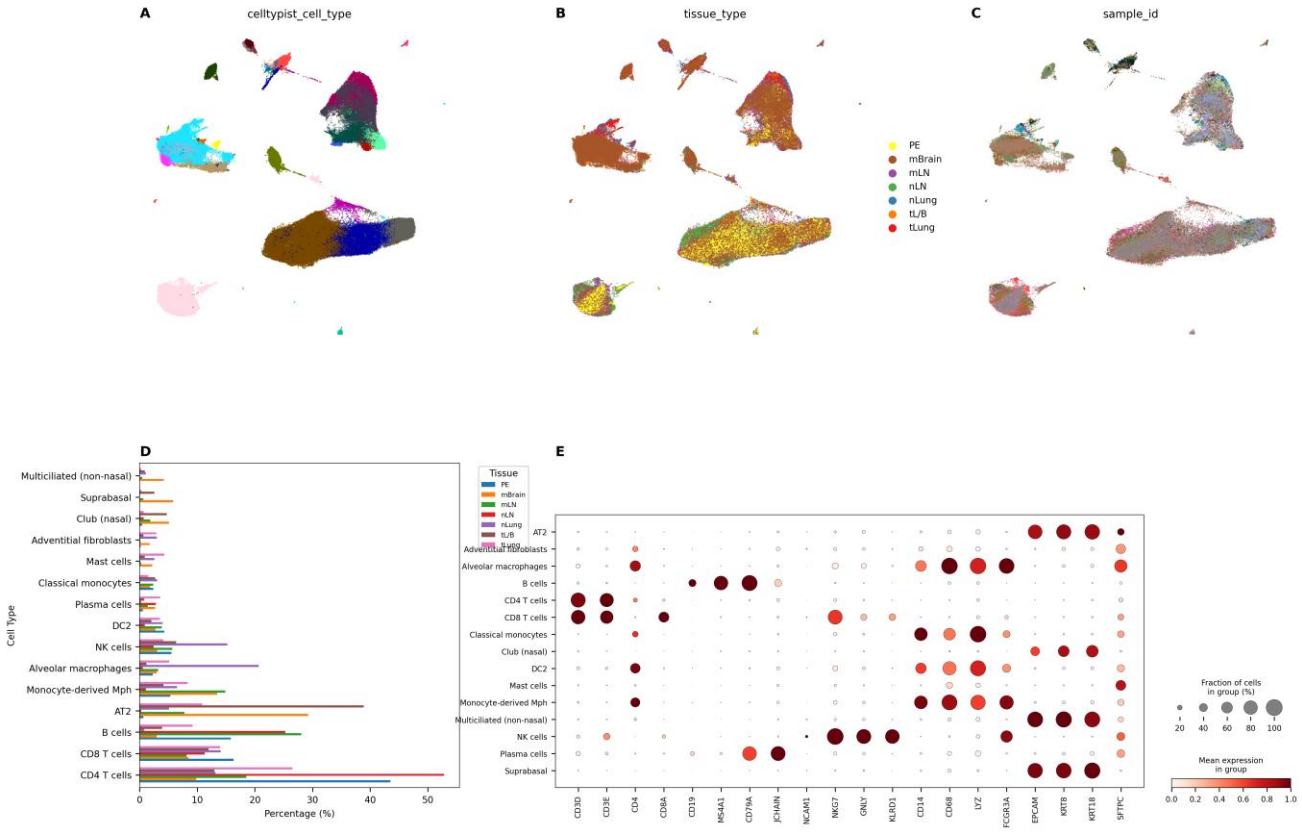


Figure 1: Single-cell atlas of NSCLC TME. (a) UMAP colored by CellTypist cell-type annotations. (b) UMAP colored by tissue type. (c) UMAP colored by sample ID. (d) Cell-type composition across tissue types for the most abundant populations. (e) Marker-gene dot plot supporting major lineage annotations.

LIANA identifies extensive intercellular communication networks

To characterize intercellular communication in the TME of NSCLC, we utilized LIANA[14], a framework that integrates multiple established inference methods (CellPhoneDB, Connectome, NATMI, SingleCellSignalR, and CellChat) to identify high-confidence ligand–receptor interactions. This multi-method consensus approach identified 195,143 candidate ligand–receptor pairs across all cell type combinations (Fig. 2a-c, Supplementary Data 2).

The highest-ranked global LIANA interactions included inflammatory signaling from myeloid cells to epithelial populations. Classical monocytes showed high-confidence predicted signaling to AT1 cells through S100A8–AGER and S100A9–AGER interactions (magnitude rank < 0.01), representing damage-associated molecular pattern (DAMP) signaling that may drive epithelial injury and tissue remodeling (Supplementary Data 2). Similarly, proliferating T cells communicated with AT1 cells via HMGB1–AGER, an additional DAMP pathway implicated in tissue damage responses.

Immune cell interactions were frequently mediated by major histocompatibility complex (MHC) class I recognition. Endothelial cells, NK cells, and $CD8^+$ T cells engaged through B2M–KLRD1 interactions,

indicating active immune surveillance (Supplementary Data 2). T cell–B cell interactions encompassed multiple co-stimulatory and cytokine signals, including CD40–CD40LG, IL-2–IL-2RA/IL-2RB, and IFNG–IFNGR1/IFNGR2, supporting coordinated adaptive immune responses.

Stromal–immune interactions revealed extensive communication between fibroblasts and immune cells. Both adventitial and alveolar fibroblasts signaled to macrophages through collagen–integrin interactions (COL1A1–ITGB1, COL1A2–ITGB1) and chemokine signaling (CXCL12–CXCR4), which may regulate macrophage recruitment and polarization in fibrotic niches (Supplementary Data 2).

Signaling associated with epithelial repair was apparent via multiple pathways in the communication between AT2 proliferating cells and multiciliated cells, including tissue remodeling factors (TIMP1–CD63), adenosine-mediated immunosuppression (ADO–ADORA2B), and stem cell maintenance signals (LIF–IL6ST/LIFR), pointing to coordinated epithelial regeneration programs (Supplementary Data 2). Figure 2 summarizes the global communication landscape by showing the top interaction network, source-target interaction counts, incoming and outgoing interaction burdens, recurrent ligands, the highest-ranked interaction pairs, and the spatial co-localization distribution of the filtered subset (Fig. 2a-f).

The identities of recurrent ligands, receptors, and source-target cell type pairs were consistent with immune regulation, antigen presentation, extracellular matrix remodeling, and epithelial repair programs. Because pathway enrichment of ligand-receptor classes was not used as a primary discovery step, these functional assignments should be interpreted as annotation-guided biological interpretations rather than independent pathway-enrichment results.

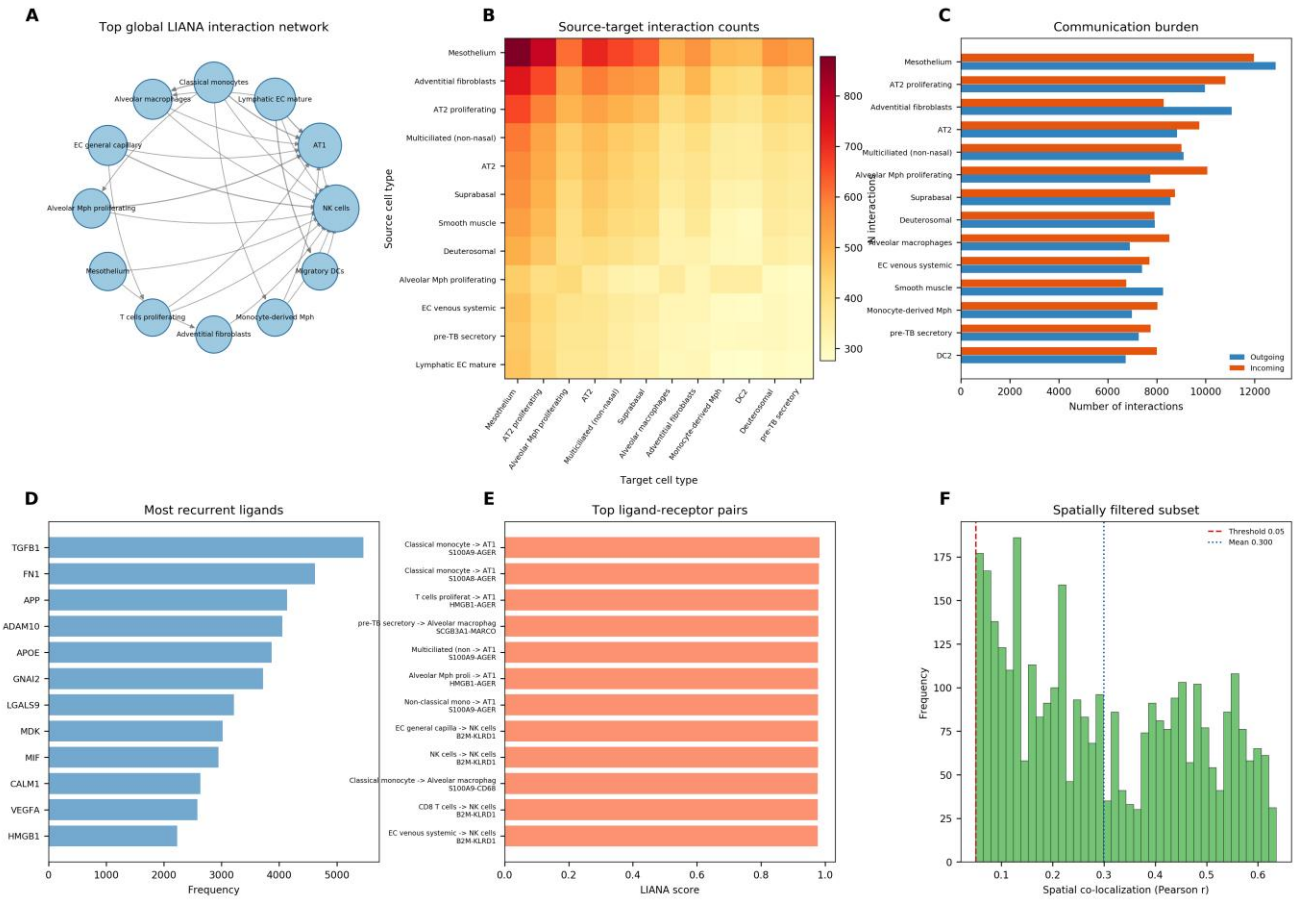


Figure 2: Global LIANA cell-cell communication networks. (a) Directed network of the top-ranked LIANA interactions. (b) Source-target interaction count heatmap for the most connected cell types. (c) Incoming and outgoing interaction counts by cell type. (d) Most recurrent ligands across candidate interactions. (e) Top ligand-receptor interactions ranked by LIANA score. (f) Spatial co-localization distribution when spatially filtered interactions are available; the spatially constrained subset is analyzed in detail in Figure 5.

Spatial transcriptomics delineates sample-specific microenvironmental domains

To determine how cell types are spatially organized in intact tissue, we analyzed spatial transcriptomics data from six Visium samples (19,039 spots in total: 1 original sample comprising 3,816 spots and 5 GSE189487 samples comprising 15,223 spots). The primary spatial section was segmented into spatial clusters with neighborhood-aware clustering, and the implemented workflow used Leiden cluster labels when BANKSY-domain labels were not available in the stored object (Fig. 3a). The resulting spatial clusters showed distinct cellular compositions and spatial distributions (Fig. 3c-d, Supplementary Fig. 3a).

Domain characterization through cell2location deconvolution revealed functionally distinct microenvironmental niches (Fig. 3c, Supplementary Table 2). Several clusters were enriched in airway

or alveolar epithelial populations (including AT2, AT2 proliferating, Club, deuterosomal, and multiciliated cells), whereas others showed increased smooth muscle, plasma cell, fibroblast, endothelial, or myeloid abundance. These patterns indicate that the spatial clusters capture major epithelial, immune, stromal, and vascular tissue structures rather than arbitrary expression partitions.

Spatially variable gene (SVG) analysis using Moran's I identified 2,967 genes with significant spatial autocorrelation (FDR < 0.05) (Supplementary Data 3). The top SVGs included immune markers (CD8A, CD4, MS4A1), epithelial markers (SFTPC, AGER), and stromal markers (COL1A1, COL1A2), confirming spatial segregation in major cell lineages. Spatial maps of representative marker genes further supported the interpretation that these domains correspond to immune, epithelial, and stromal tissue structures (Supplementary Fig. 3c).

Cross-sample analyses across all six Visium sections showed recurrent but sample-specific spatial organization, including recovery of major spatial communication modules and selected immune and epithelial-repair states despite substantial sample-to-sample heterogeneity (Fig. 10a-c; Supplementary Data 7-8). We therefore interpret the spatial domains and communication patterns as reproducible organizational features with variable prevalence across sections, rather than as one fixed set of universal regions across all samples.

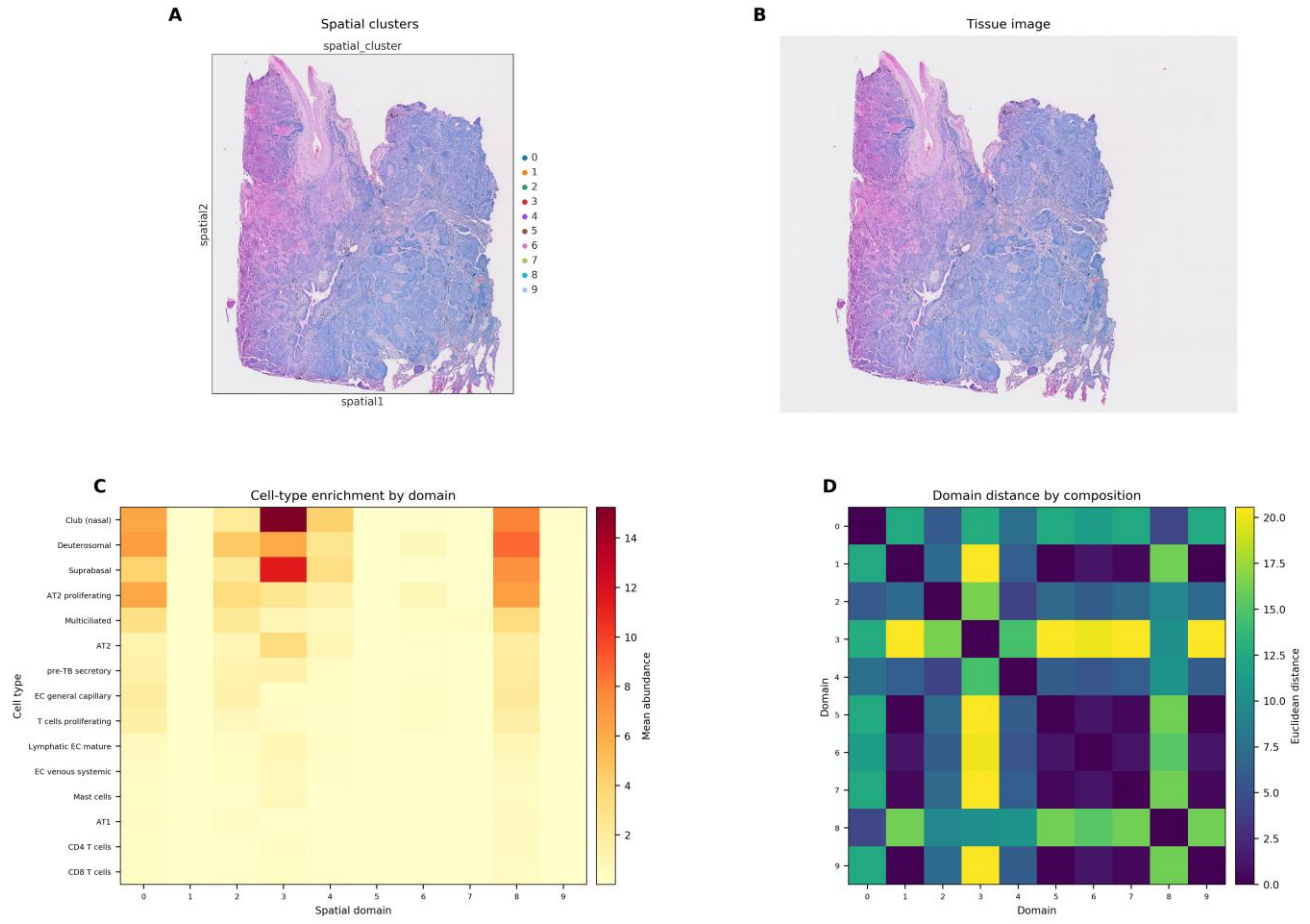


Figure 3: Spatial domain organization in the primary Visium section. (a) Spatial cluster map over tissue coordinates. (b) Tissue image corresponding to the spatial section. (c) Cell-type enrichment across spatial domains estimated by cell2location. (d) Pairwise distance matrix between spatial domains based on cell-type composition. Spatially variable genes are provided in Supplementary Data 3 and Supplementary Fig. 3c; cross-sample recurrence checks are summarized in Figure 10 and Supplementary Data 7-8.

Cell2location deconvolution enables high-resolution spatial cell type mapping

To resolve cell types at spot level in these spatial domains, we applied cell2location[13], a Bayesian deconvolution method that estimates cell type composition of spatial transcriptomics spots with scRNA-seq reference profiles (Fig. 4a). Trained on our 31-cell-type scRNA-seq atlas, cell2location estimated cell type abundances across all 19,039 spots (Fig. 4b-c, Supplementary Fig. 4a).

Cell2location revealed distinct spatial distribution patterns for individual cell types (Fig. 4b-d). T lymphocytes ($CD4^+$, $CD8^+$, and proliferating T cells) clustered in immune-infiltrated regions, frequently co-localizing with B cells and plasma cells. Macrophage populations showed distinct spatial preferences: alveolar macrophages were enriched in alveolar-like regions, whereas monocyte-derived macrophages were concentrated in distinct stromal and immune-associated niches. Epithelial cells (AT1, AT2, Club, and multiciliated) displayed complementary spatial distributions, with AT2 cells enriched in alveolar regions and Club/multiciliated cells localized to airway-associated structures. A dominant-cell-type map further summarized the inferred local cellular composition across spots (Fig. 4c).

Notably, plasma cells showed focal clustering patterns in the spatial abundance maps and cell-type co-localization matrix (Fig. 4b,d), with high local densities in discrete regions, suggesting TLS-like organization. Fibroblast subtypes displayed spatial segregation, with adventitial fibroblasts enriched in perivascular-like regions and alveolar fibroblasts distributed across stromal regions.

Cell2location estimation showed strong agreement with canonical marker gene expression, with a median Pearson correlation of 0.71 across all 31 cell types (range: 0.52–0.82; Supplementary Fig. 4d). Cell2location also successfully resolved rare cell types (e.g., mast cells and plasmacytoid DCs) that would be challenging to detect through marker gene expression alone, demonstrating the utility of reference-based deconvolution.

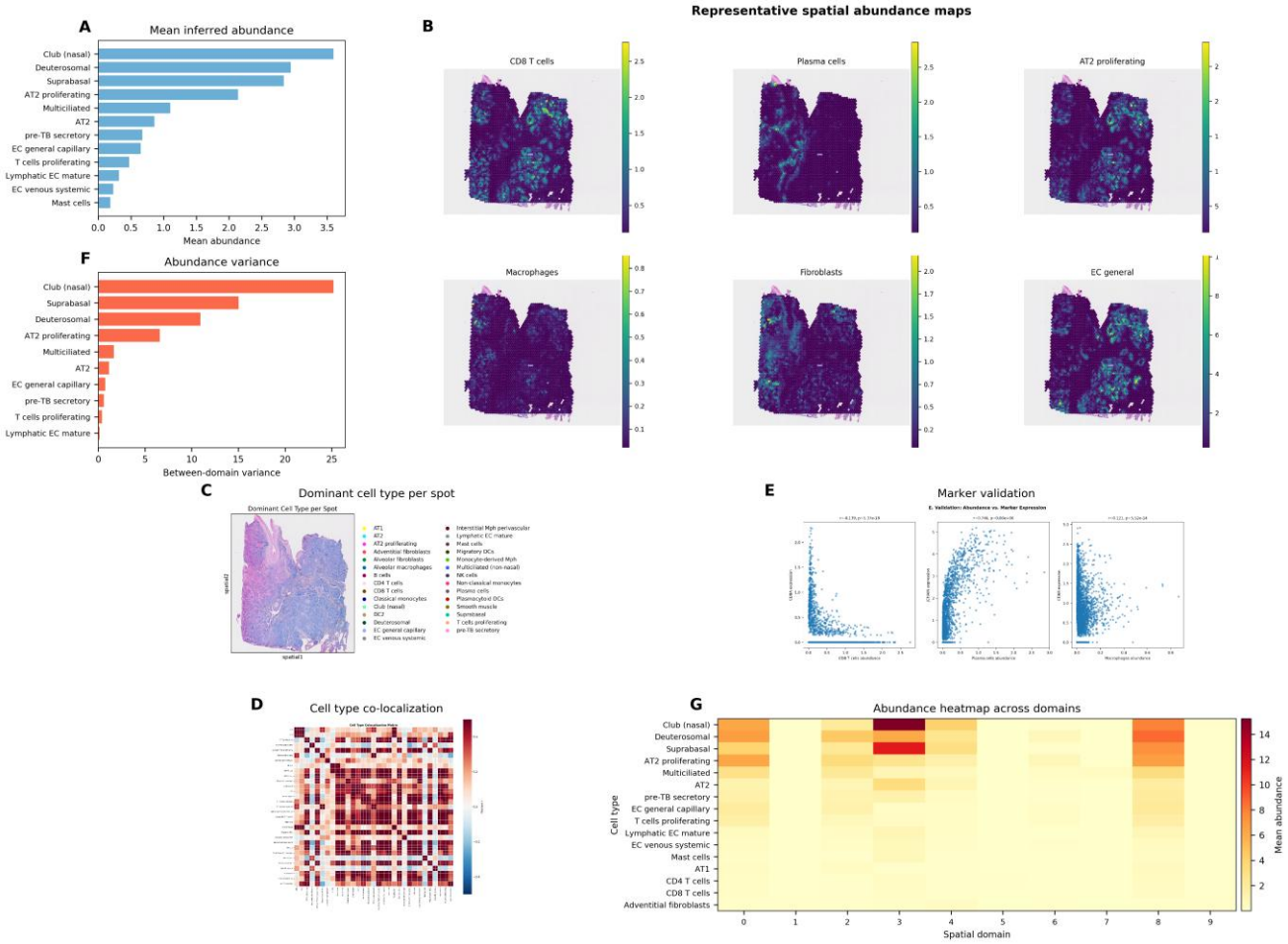


Figure 4: Cell2location-based spatial cell type mapping. (a) Mean abundance of the most abundant inferred cell types. (b) Spatial abundance maps for representative cell types. (c) Dominant inferred cell type per spot. (d) Cell-type co-localization matrix based on inferred abundance profiles. (e) Validation of inferred abundance against canonical marker gene expression. (f) Cell-type abundance variance across spatial domains. (g) Abundance heatmap for the top inferred cell types across spatial domains.

Spatial co-localization analysis identifies candidate communication networks

After mapping cell type distributions across tissue, we integrated LIANA interaction scores with spatial co-localization analysis (Fig. 5a). For each ligand-receptor pair, we computed the Pearson correlation between source and target cell type abundances across all spots as a measure of spatial co-localization (Fig. 5b, Methods). Filtering the top 5,000 LIANA interactions for those with co-localization scores >= 0.05 yielded 3,451 spatially constrained interactions (Fig. 5a-c, Supplementary Data 4). Permutation testing (500 permutations with random shuffling of spot identities) confirmed that 3,348 of these (97.0%) were statistically significant at FDR < 0.05, and 3,067 (88.9%) at FDR < 0.01. The observed spatial co-localization patterns thus significantly exceed random expectation (mean z-score = 7.9).

The highest LIANA-ranked interactions retained after spatial filtering included classical monocyte to AT1 cell signaling via S100A8/S100A9–AGER (Pearson r = 0.059), consistent with an inflammatory DAMP

signaling hypothesis, although this pair showed only modest single-section permutation support (FDR = 0.069). Notably, AT2 proliferating to multiciliated cell interactions formed the top co-localized interaction class (r = 0.636; Fig. 5c,e), with THBS1–SCARB1 representing one epithelial repair-associated ligand-receptor pair within this tied group. Thus, S100A8/A9–AGER emerged as the top LIANA-confidence interaction passing the spatial co-localization threshold, whereas the AT2 proliferating to multiciliated cell program represented the strongest spatial co-localization class (Supplementary Fig. 5a).

Representative highly co-localized interactions included:

- AT2 proliferating cells → multiciliated cells (THBS1–SCARB1, r = 0.636): one of the tied top epithelial repair-associated signals
- Endothelial cells → NK cells (B2M–KLRD1, r = 0.089): MHC class I-mediated immune recognition
- Fibroblasts → macrophages (COL1A1–ITGB1, r = 0.076): extracellular matrix–integrin interactions
- B cells → T cells (CD40–CD40LG, r = 0.068): co-stimulatory signaling

Network analysis of spatially constrained interactions highlighted recurrent source-target pairs and cell type groups with dense spatially supported communication (Fig. 5a,f). Classical monocytes, DC2 cells, endothelial cells, epithelial populations, and macrophage subsets appeared repeatedly among the spatially filtered interactions, consistent with their roles as candidate organizers of TME structure.

The top co-localized interaction class was epithelial repair-associated AT2 proliferating to multiciliated cell communication, and the representative source-cell spatial map showed that this signal was concentrated in a subset of the tissue section (Fig. 5e). The most frequent spatially constrained cell type pairs included macrophage, epithelial, lymphatic endothelial, and T cell axes (Fig. 5f), indicating that spatial filtering prioritizes cell type pairs that share local tissue niches.

Sensitivity analysis across co-localization thresholds confirmed the stability of the filtered interaction set: threshold 0.05 yielded 3,451 interactions, 0.08 yielded 3,107, 0.10 yielded 2,928, and 0.15 yielded 2,515, with the top-ranked interactions (including S100A8/A9–AGER) consistently recovered across all thresholds (Supplementary Fig. 5f). We selected 0.05 as the primary threshold to balance sensitivity with specificity, retaining interactions with meaningful spatial co-occurrence while excluding noise.

Comparison of LIANA score and spatial co-localization showed that the two quantities were only weakly related in the spatially filtered set (Fig. 5g). Many highly ranked LIANA interactions had modest spatial co-localization, suggesting indirect or tissue-architecture-driven signals rather than local cell-cell communication. Conversely, several moderately ranked interactions displayed high spatial co-localization, implying potential local relevance despite lower expression-based confidence.

The ligand-receptor pairs that appeared most frequently after spatial filtering included HLA-A-APLP2, TIMP1-CD63, VIM-CD44, APP-CD74, HMGB1-CXCR4, and LGALS1-integrin interactions (Fig. 5h).

Multi-sample spatial analyses supported recurrent cell-composition structure across sections, but sample-specific variation remained substantial (Fig. 10), so the spatially constrained interactions should be interpreted as candidate local communication events requiring validation.

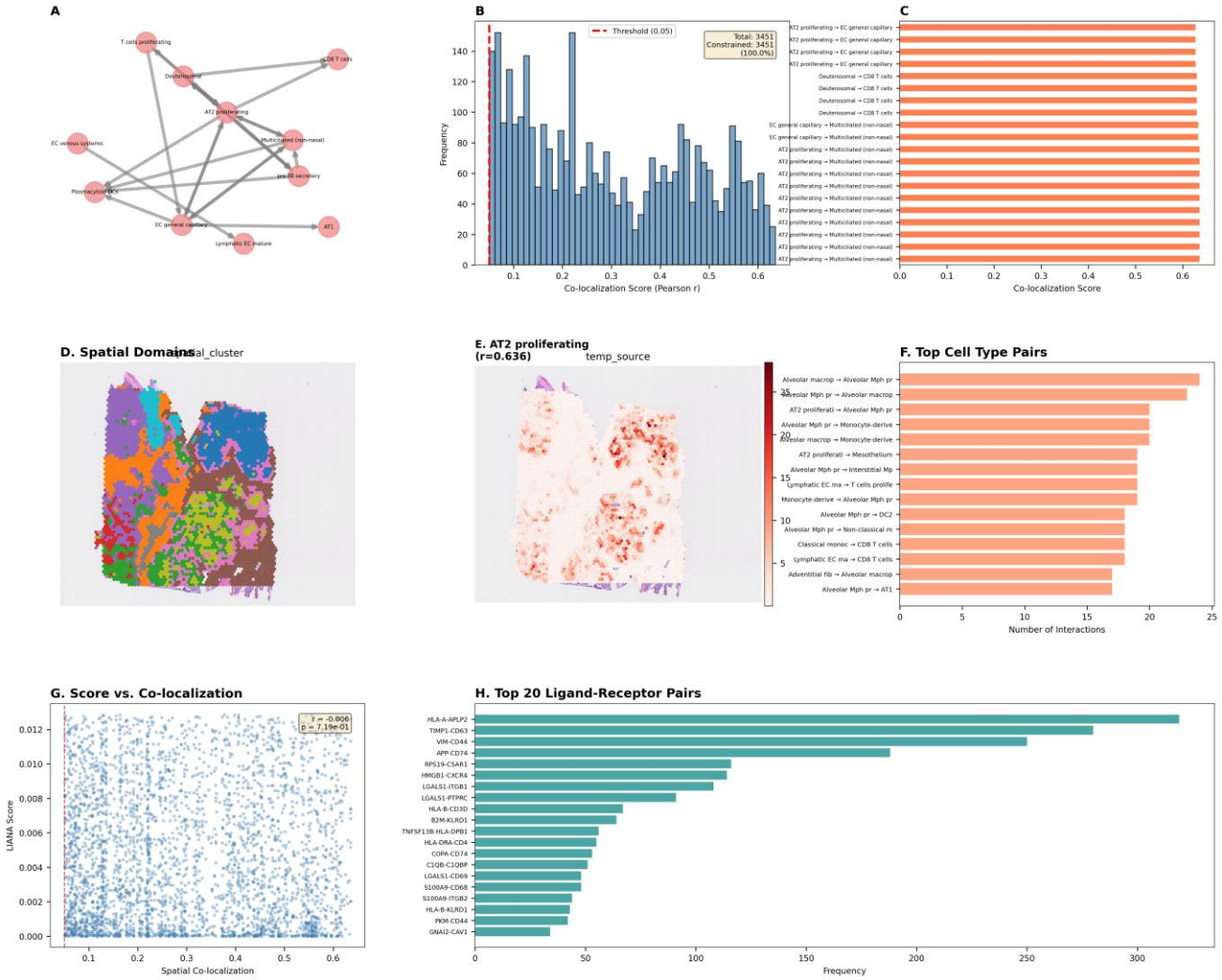


Figure 5: Spatially constrained communication. (a) Network of top spatially constrained LIANA interactions. (b) Distribution of spatial co-localization scores with the 0.05 threshold. (c) Top interactions ranked by spatial co-localization. (d) Spatial domain map for the analyzed section. (e) Spatial distribution of the source cell type for a representative top co-localized interaction class. (f) Most frequent source-target cell type pairs among spatially constrained interactions. (g) LIANA score versus spatial co-localization. (h) Most frequent ligand-receptor pairs after spatial filtering.

Spatial autocorrelation reveals cell type clustering patterns and TLS signatures

Beyond pairwise co-localization, we examined whether individual cell types form spatially coherent clusters. We computed Moran's I spatial autocorrelation statistics for each of the 31 cell type abundance

profiles (Fig. 6a, Methods). All cell types showed statistically significant positive spatial autocorrelation (permutation $p < 0.05$ after FDR correction), indicating non-random spatial distributions (Supplementary Data 5).

Smooth muscle cells displayed the highest spatial autocorrelation (Moran's I = 0.627), consistent with their organization into continuous bronchial and vascular structures (Fig. 6b). Adventitial fibroblasts (I = 0.458) and alveolar fibroblasts (I = 0.392) also showed high autocorrelation, in accordance with their roles in forming stromal niches.

Among immune cells, plasma cells exhibited notable spatial autocorrelation (I = 0.080 in multi-sample analysis; I = 0.474 in the original single sample), consistent with TLS-like organization (Fig. 6b-c). B cells (single-sample I = 0.233; multi-sample I = 0.021) and T cell subsets (single-sample $CD4^+$ T cells, I = 0.284; $CD8^+$ T cells, I = 0.326; multi-sample $CD4^+$ T cells, I = 0.281; $CD8^+$ T cells, I = 0.493) also demonstrated spatial clustering. The attenuated plasma cell Moran's I value observed in the multi-sample analysis reflects inter-sample heterogeneity in TLS-like organization, with certain samples harboring focal plasma cell aggregates while others exhibit more diffuse immune infiltration.

Epithelial cells displayed moderate-to-high spatial autocorrelation (AT2, I = 0.371; AT1, I = 0.311; multiciliated, I = 0.391), concordant with their organization into alveolar and airway structures. Endothelial cell subtypes also showed spatial autocorrelation (general capillary, I = 0.401; venous systemic, I = 0.408), reflecting vascular network architecture.

Myeloid cells also showed significant spatial autocorrelation (alveolar macrophages, I = 0.241; monocyte-derived macrophages, I = 0.367), consistent with structured myeloid niches rather than random tissue surveillance alone.

Pattern classification based on Moran's I values showed that cell type abundance profiles were predominantly spatially clustered rather than randomly distributed (Fig. 6d). Pairwise cell-type co-localization is shown separately in Figure 4d.

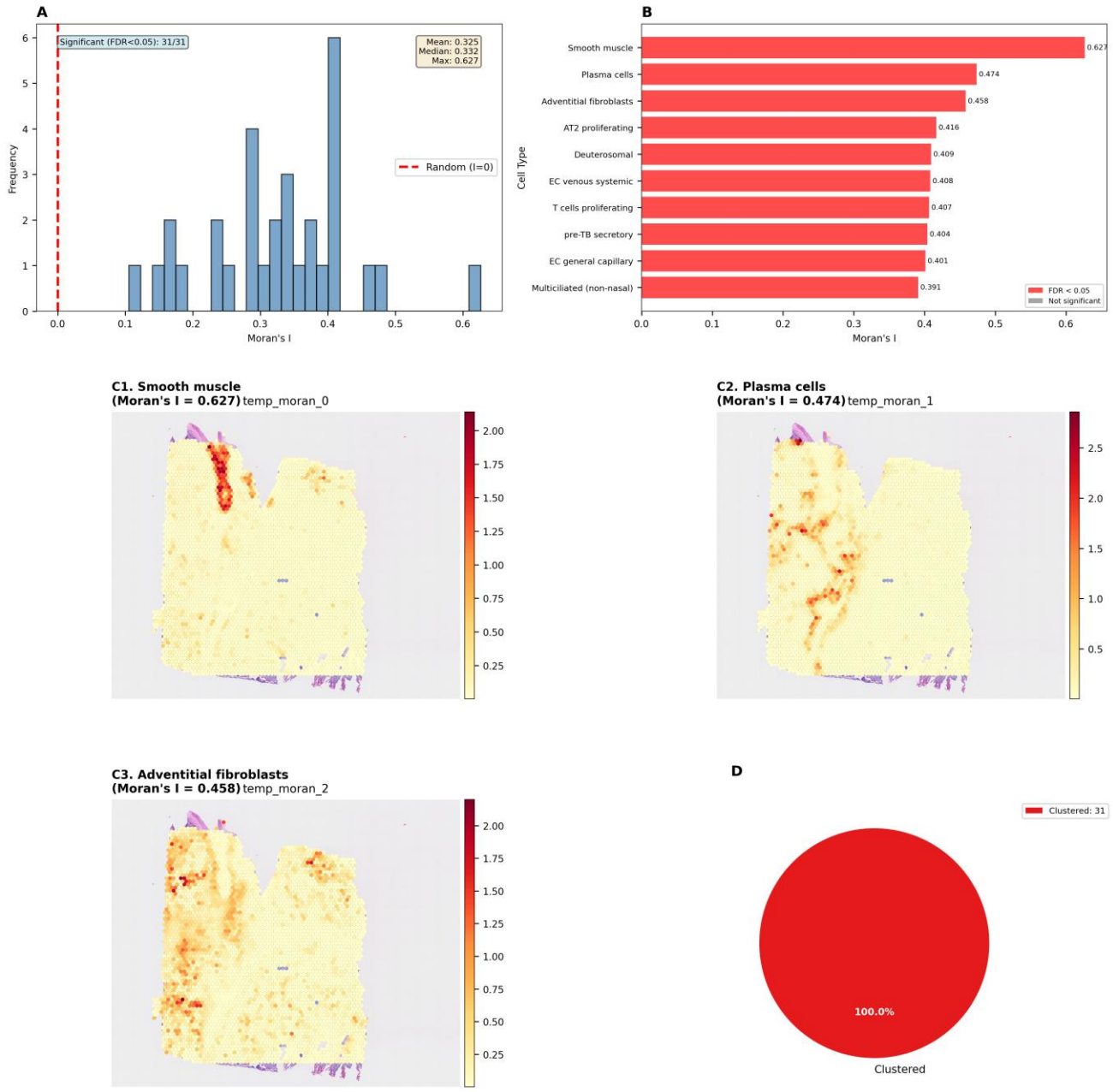


Figure 6: Spatial autocorrelation patterns. (a) Distribution of Moran's I values across inferred cell type abundance profiles. (b) Top spatially clustered cell types. (c) Spatial maps for representative high-Moran's I cell types. (d) Spatial pattern classification based on Moran's I.

T cell exhaustion exhibits spatial heterogeneity and correlates with immune infiltration density

Given the clinical importance of T cell dysfunction, we next mapped exhaustion states across tissue. We computed exhaustion scores combining inhibitory receptors (PDCD1, HAVCR2, LAG3, CTLA4, and TIGIT), exhaustion-associated transcription factors (TOX, TOX2, NR4A1, and NR4A3), minus effector

function genes (GZMB, PRF1, IFNG, and TNF) (Fig. 7a; see Methods for complete gene lists and formula). We then projected exhaustion scores with cell2location-derived T cell abundances as weights.

Spatial exhaustion mapping revealed substantial heterogeneity across tissue regions (Fig. 7a). Exhaustion-associated genes varied across T and NK cell populations (Fig. 7b), and the composite exhaustion score correlated positively with checkpoint gene expression, particularly CTLA4, TIGIT, and PDCD1 (Fig. 7c). Domain-level analysis showed that exhaustion scores differed across spatial domains, with the highest values observed in one spatial domain with prominent immune-associated signal (Fig. 7d).

The spatial exhaustion score was significantly associated with immune infiltration density, although the relationship was not simply monotonic (Fig. 7e). This pattern suggests that exhaustion is shaped by local immune context and tissue architecture rather than by total immune abundance alone.

Sample-level analysis confirmed heterogeneity in exhaustion-associated features across clinical groups and tissue sites (Supplementary Fig. 6a-c). These analyses support spatially heterogeneous T cell dysfunction while emphasizing that absolute exhaustion levels vary between samples.

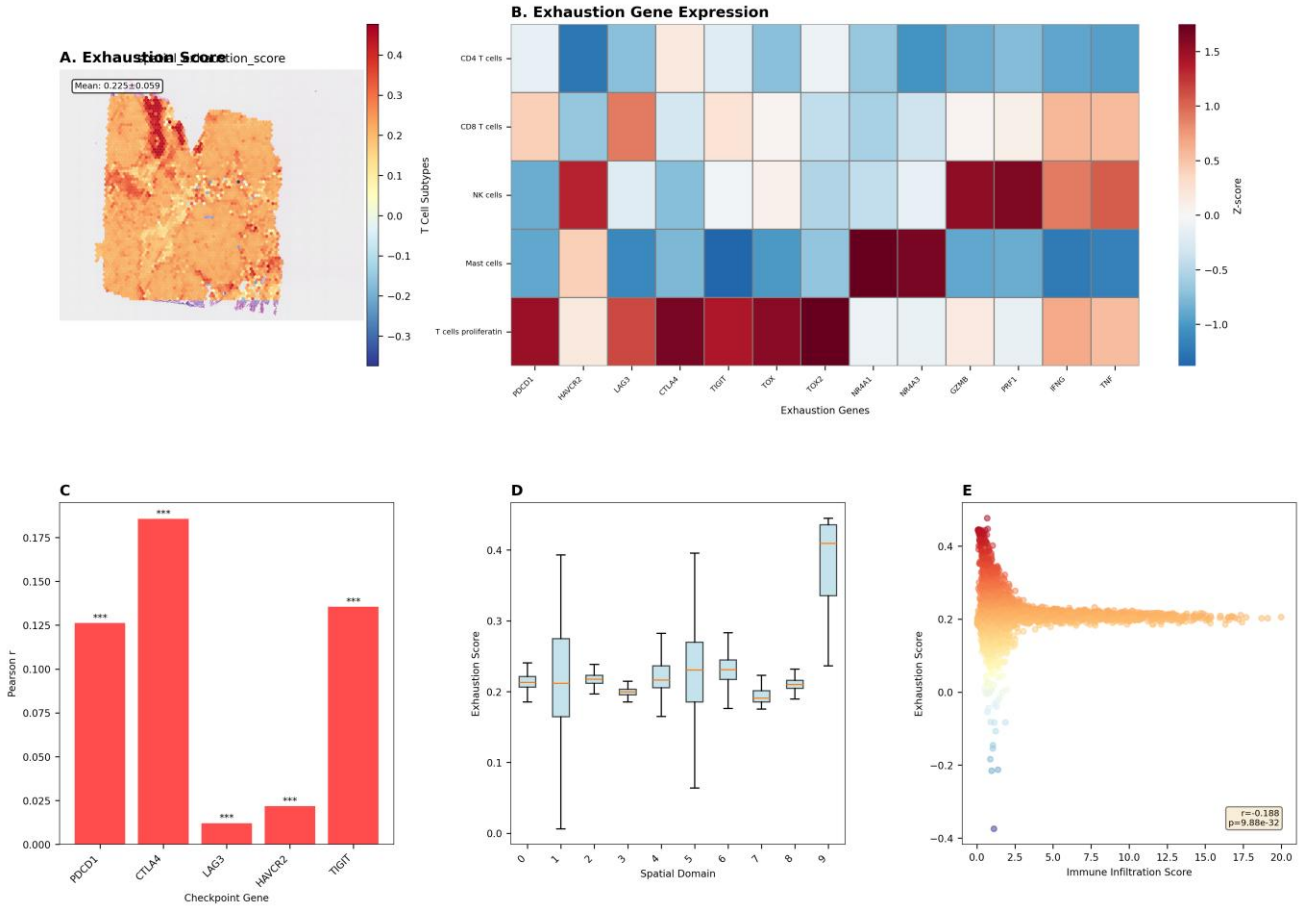


Figure 7: T cell exhaustion spatial distribution. (a) Spatial map of composite exhaustion scores. (b) Exhaustion and effector gene expression heatmap across T/NK populations. (c) Correlation between exhaustion score and

checkpoint gene expression. (d) Domain-specific exhaustion score distributions. (e) Exhaustion score versus immune infiltration score.

Clinical stage and tissue origin jointly shape TME composition

To link spatial TME features with clinical outcomes, we integrated clinical staging information extracted from GEO series matrix data and compared early-stage (I–II) and late-stage (III–IV) tumors (Fig. 8a). Of the 37 tumor samples, 9 were early-stage, all primary lung tumor (tLung), and 28 were late-stage, comprising 2 tLung, 10 metastatic brain, 7 metastatic LN, 5 pleural effusion, and 4 tumor LN. Critically, this stage distribution is confounded by tissue origin: early-stage samples are exclusively primary tumors, whereas the majority of late-stage samples derive from metastatic sites. We therefore interpret the following comparisons as reflecting combined effects of disease stage and tissue site, rather than stage alone.

Cell type proportion analysis identified nine cell types with statistically significant abundance differences between stages (Mann–Whitney U test, FDR < 0.05) (Fig. 8a-b, Supplementary Data 6). All nine showed higher abundances in early-stage (primary) relative to late-stage (predominantly metastatic) samples:

- AT1 cells: $\log_2$FC = −5.92 (early > late), consistent with the absence of alveolar epithelium at metastatic sites
- Mast cells: $\log_2$FC = −2.32, reflecting tissue-resident mast cell depletion at metastatic locations
- Migratory DCs: $\log_2$FC = −1.53, suggesting reduced antigen presentation capacity
- Lymphatic EC mature cells: $\log_2$FC = −1.09, suggesting lymphovascular remodeling
- pre-TB secretory cells: $\log_2$FC = −2.72, consistent with depletion of airway epithelial programs at metastatic sites
- Interstitial Mph perivascular cells: $\log_2$FC = −1.65, indicating altered perivascular myeloid niches
- Smooth muscle cells: $\log_2$FC = −2.05, reflecting site-specific stromal architecture
- Venous EC cells: $\log_2$FC = −1.73, indicating vascular composition shifts
- Alveolar fibroblasts: $\log_2$FC = −0.93, consistent with loss of lung-resident stromal components

These differences reflect both potential stage-associated remodeling and the fundamentally distinct microenvironments of primary versus metastatic sites. The dramatic reduction of lung-restricted epithelial and stromal populations is particularly attributable to tissue-of-origin differences rather than tumor-intrinsic immune exclusion alone (Fig. 8b-c).

Sample-level exhaustion analysis across stages yielded a paradoxical pattern in the saved feature matrix. Early-stage primary tumors displayed higher mean exhaustion scores than late-stage,

metastatic-enriched samples (0.324 versus 0.152; mean high-exhaustion cell fraction, 0.370 versus 0.205). This observation may reflect either: (1) earlier initiation of T cell dysfunction in primary tumors where antigen exposure is maximal, or (2) different T cell states at metastatic sites where immune-desert phenotypes predominate. Because Figure 8 focuses on cell-type composition and tissue-origin confounding, this exhaustion comparison is shown in Supplementary Fig. 6 and should be interpreted cautiously.

Tissue origin analysis confirmed that anatomical site is a major determinant of TME composition (Fig. 8c-d). Primary lung tumor samples retained lung-resident epithelial and stromal populations, whereas metastatic brain, metastatic lymph node, pleural effusion, and tumor lymph node samples showed distinct cell-composition profiles. This tissue-origin imbalance is the dominant caveat for interpreting the stage-associated comparisons.

Figure 8. Clinical Stage and Tissue Origin Jointly Shape TME Composition

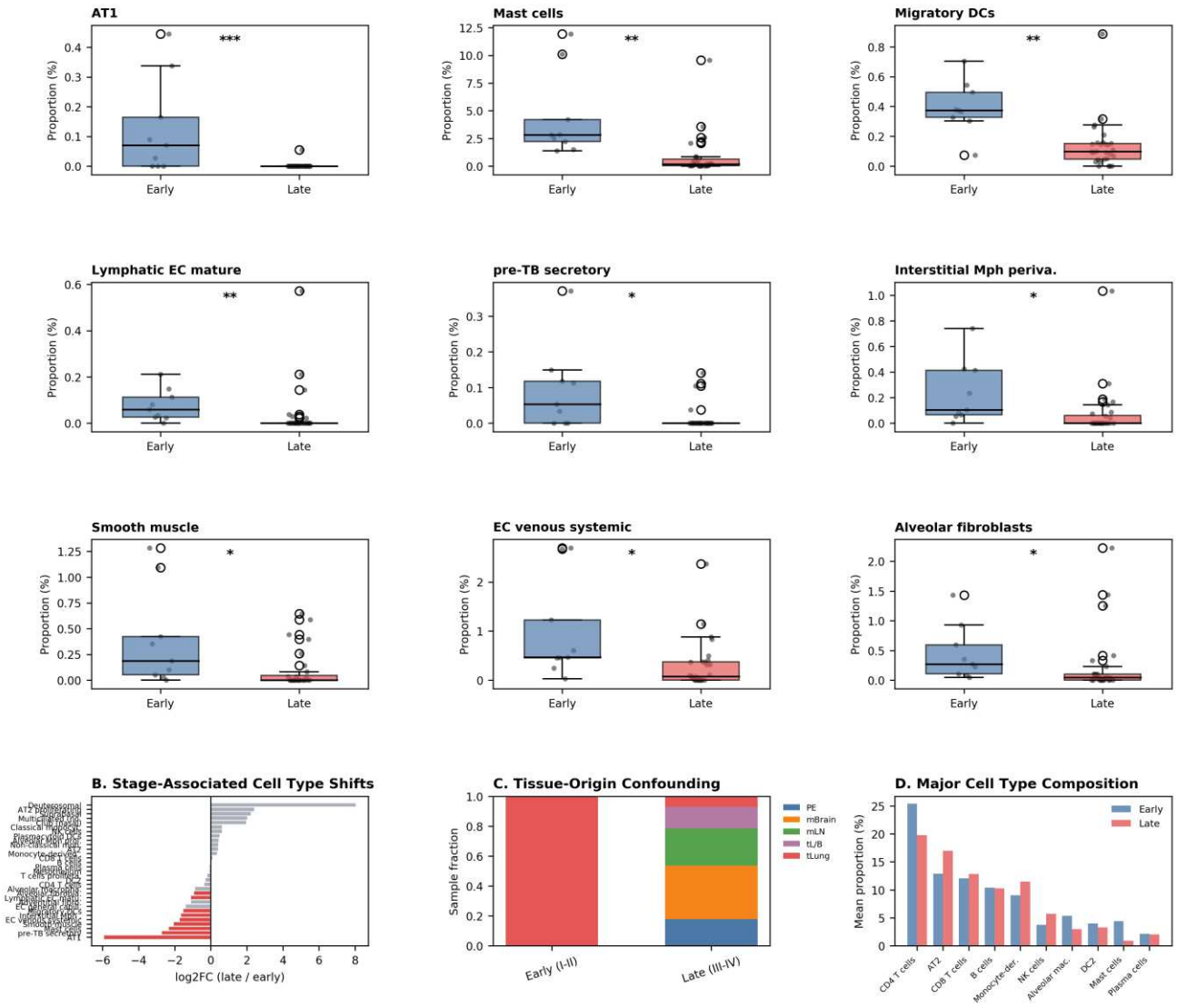


Figure 8: Clinical stage and tissue origin jointly shape TME composition. (a) Boxplots for the nine cell types significantly different between early-stage primary tumors and late-stage metastatic-enriched samples. (b) Ranked log2 fold changes for all tested cell types, highlighting FDR-significant populations. (c) Tissue-origin composition by stage group, showing strong confounding. (d) Major cell type composition by stage group.

Machine learning identifies TME cellular composition as a predictor of clinical stage

Finally, we asked whether cellular-composition-derived TME features can distinguish disease stage. We developed a machine learning framework to predict clinical stage (early versus late) using cell type proportions together with myeloid, stromal, and vascular summary features, deliberately excluding T cell exhaustion-derived features to avoid circular reasoning (Methods).

We extracted 41 features per sample, comprising:

- Cell type proportions (31 features)
- Myeloid polarization scores (M1/M2 ratio and subtype-specific scores: 5 features)
- Stromal and vascular metrics (5 features)

Of the 37 tumor samples with complete feature data, 9 were early-stage (I–II) and 28 were late-stage (III–IV) (Fig. 9a). An XGBoost classifier trained with five-fold cross-validation achieved high apparent predictive performance (mean AUC = 0.930 ± 0.098) (Fig. 9b), suggesting that TME cellular composition contains strong information about stage group and tissue origin.

SHAP (SHapley Additive exPlanations) analysis, computed via TreeExplainer on a companion Random Forest classifier (see Methods), identified the most informative predictive features (Fig. 9c–d):

1. Migratory DC proportion (SHAP value = 0.057): the highest-ranked feature, indicating that antigen presentation capacity distinguishes disease stages
2. Mast cell proportion (SHAP value = 0.044): the second-ranked feature, implicating innate immune contributions
3. AT1 cell proportion (SHAP value = 0.041): associated with epithelial differentiation state
4. Lymphatic EC proportion (SHAP value = 0.028): suggesting lymphovascular remodeling
5. Venous EC proportion (SHAP value = 0.020): representing vascular architecture changes

Notably, the top predictive features (migratory DCs and mast cells) overlap with immunotherapy-relevant tumor immune states described in independent cohorts[25],[26]. These associations suggest translational hypotheses but do not establish ICI response prediction in the present cohort. Several stromal and vascular features, including smooth muscle cells, interstitial macrophages, and endothelial populations, also contributed to the model, consistent with coordinated tissue-site and stage-associated remodeling.

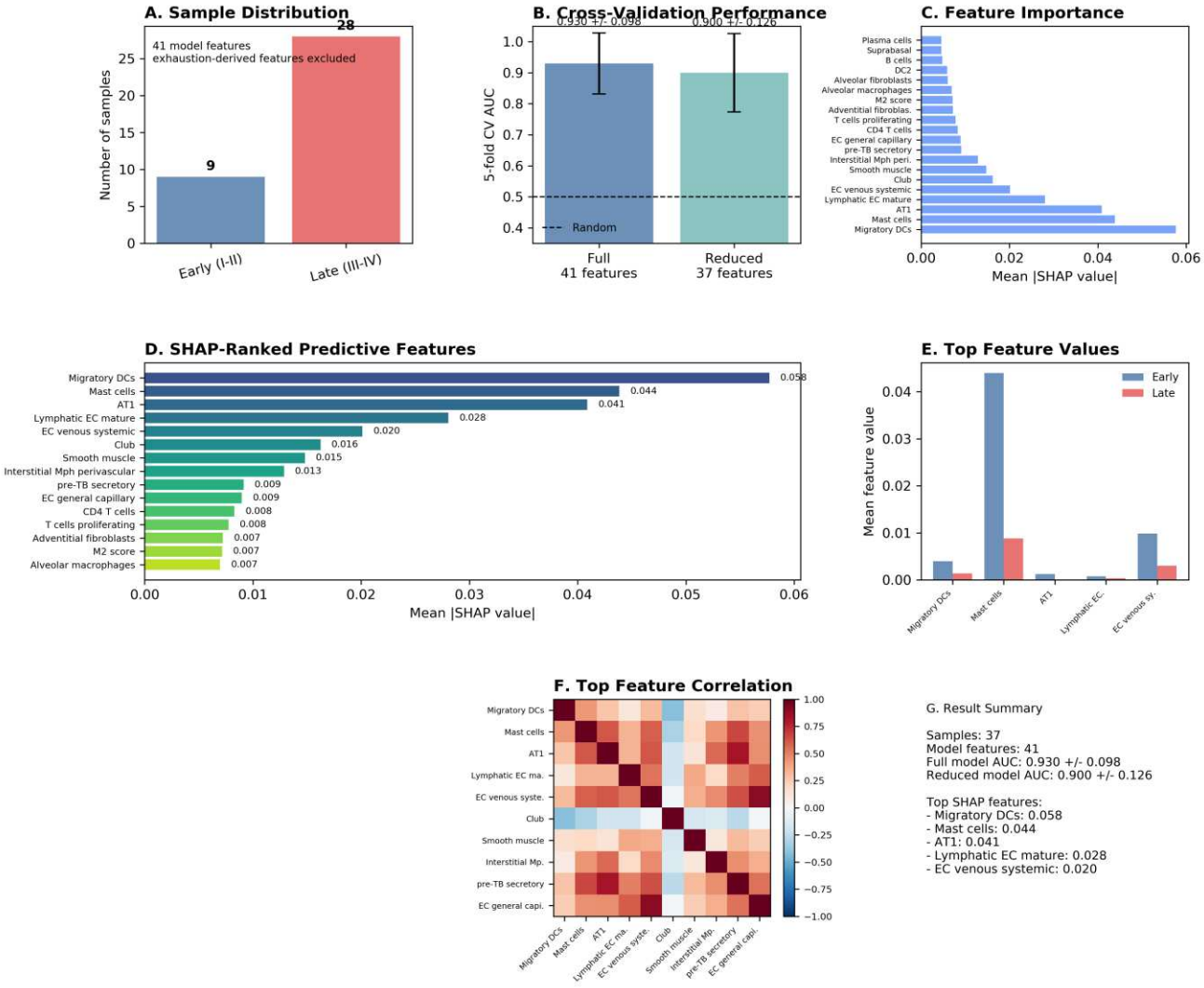
Group-wise feature summaries showed that early-stage primary tumors had higher mean migratory DC and mast cell proportions than late-stage metastatic-enriched samples, whereas several epithelial, stromal, and vascular features also differed by stage group. These patterns should be interpreted as combined stage and tissue-origin effects rather than pure stage biology.

To assess the potential confounding effect of tissue origin on model performance, we retrained the classifier after excluding four tissue-specific features (AT1 cells, alveolar macrophages, Club cells, and multiciliated cells, populations anatomically restricted to the lung). The reduced model (37 features) retained high apparent performance (AUC = 0.900 ± 0.126), a modest decrease from the full model (AUC = 0.930 ± 0.098), indicating that predictive power is not explained solely by these four lung-

restricted populations. However, residual tissue-origin confounding remains likely because stage and anatomical site are strongly coupled in this cohort.

To assess translational implications, we examined the overlap between stage-predictive features and known immunotherapy-relevant immune states. Among the top 10 features, migratory DCs and mast cells have been independently associated with tumor immune phenotypes in prior studies[25],[26], while additional ranked immune and stromal features may reflect tissue-site and stage-associated remodeling. These observations support hypotheses about immune-state differences across stage and tissue-site groups, but prospective validation in ICI-treated NSCLC cohorts would be required before any therapeutic predictive claim can be made.

Figure 9. Machine Learning Prediction of Clinical Stage



AUC values are reported cross-validation summaries from the saved analysis; fold-level ROC predictions are not stored in the repository.

Figure 9: Machine learning prediction of clinical stage. (a) Early- and late-stage sample distribution used for model training. (b) Five-fold cross-validation AUC summary for the full 41-feature model and the reduced 37-feature model excluding lung-restricted cell types. (c) Top 20 feature importance values. (d) SHAP-ranked predictive features. (e) Mean values of the top-ranked features by stage group. (f) Correlation structure among top predictive features. (g) Result summary from the saved model outputs.

Cross-sample and external anti-PD-1 validation support immunotherapy-relevant spatial immune states

To strengthen the translational relevance of the spatial findings, we performed two validation analyses. First, we compared spatially constrained communication patterns between the original discovery section and the integrated six-sample spatial dataset. The multi-sample analysis identified 4,203 spatially constrained interactions. Of these, 3,018 exact ligand-receptor interactions overlapped with the discovery-section interaction set, and 570 source-target cell type pairs were shared between the two analyses (Fig. 10a; Supplementary Data 7-8). Notably, all top 20 source-target pairs ranked by discovery-section co-localization were recovered in the multi-sample analysis, supporting recurrence of the major spatial communication modules despite sample-to-sample heterogeneity.

The multi-sample validation also supported recurrence of key cellular states. Plasma cells showed strong focal clustering in the original Visium section (Moran's I = 0.474) and weaker but significant clustering in the six-sample analysis (Moran's I = 0.080; Fig. 10b), consistent with heterogeneous TLS-like organization across samples. AT2 proliferating, multiciliated, B-cell, plasma-cell, T-cell, mast-cell, and migratory DC states were detectable across the validation samples, although their abundance varied substantially (Fig. 10c). These results support a model in which spatial immune and epithelial-repair states recur across lung adenocarcinoma sections but differ in prevalence between individual tumors.

Second, we tested whether immune-state signatures derived from the spatial analysis were associated with anti-PD-1 response in an independent pretreatment NSCLC RNA-seq cohort (GSE126044; 16 patients, including 5 responders and 11 non-responders)[27]. We calculated z-score-normalized signature scores for seven candidate modules representing inflammatory S100A8/A9-AGER signaling, epithelial repair communication, TLS/plasma-B-cell organization, T cell exhaustion/checkpoint activity, migratory DC state, mast-cell state, and stromal-vascular remodeling (Methods; Supplementary Data 9-10). The T cell exhaustion/checkpoint signature was higher in responders than non-responders (mean difference = 0.987; permutation p = 0.0048; FDR = 0.033; AUC = 0.91; Fig. 10e-f). Bootstrap resampling supported this discrimination (AUC 95% CI = 0.73-1.00), and leave-one-gene-out analysis retained high AUC values (0.91-0.96; Supplementary Data 11; Supplementary Fig. 7). The TLS/plasma-B-cell organization signature also trended higher in responders (mean difference = 1.038; permutation p = 0.027; FDR =

0.094; AUC = 0.85; Fig. 10d,f), consistent with prior reports linking TLS and B-cell organization to immunotherapy response. Epithelial repair communication showed a weaker exploratory association (AUC = 0.82; FDR = 0.182), whereas the S100A8/A9-AGER inflammatory signature did not clearly distinguish responders from non-responders (AUC = 0.60; FDR = 0.821).

As an additional orthogonal check, we analyzed GSE200916, an independent Visium dataset of 12 tumor and tumor-adjacent normal samples from three multiple-primary lung cancer patients[28]. GEO provides processed expression matrices but not tissue-position files for this series, so we used the data only for spot-level signature validation rather than spatial-neighborhood inference. The TLS/plasma-B-cell organization signature showed tumor-enriched spot-level separation (oriented AUC = 0.71), although the six paired tumor-normal sample comparison was not significant (paired sign-flip p = 0.25; Supplementary Data 12-13; Supplementary Fig. 7). Together, these results provide independent, treatment-relevant support for the immune-state components of the spatial atlas while reinforcing that individual ligand-receptor candidates require functional validation.

To move beyond edge-level interpretation, we collapsed the exact recurrent overlap subset into source-target modules and ranked them with a composite score integrating LIANA confidence, spatial co-localization, and recurrence (Supplementary Data 15). This module-level view highlighted recurrent epithelial, stromal, and immune communication programs rather than isolated ligand-receptor edges.

Figure 10. Cross-sample validation and immunotherapy-relevant external validation

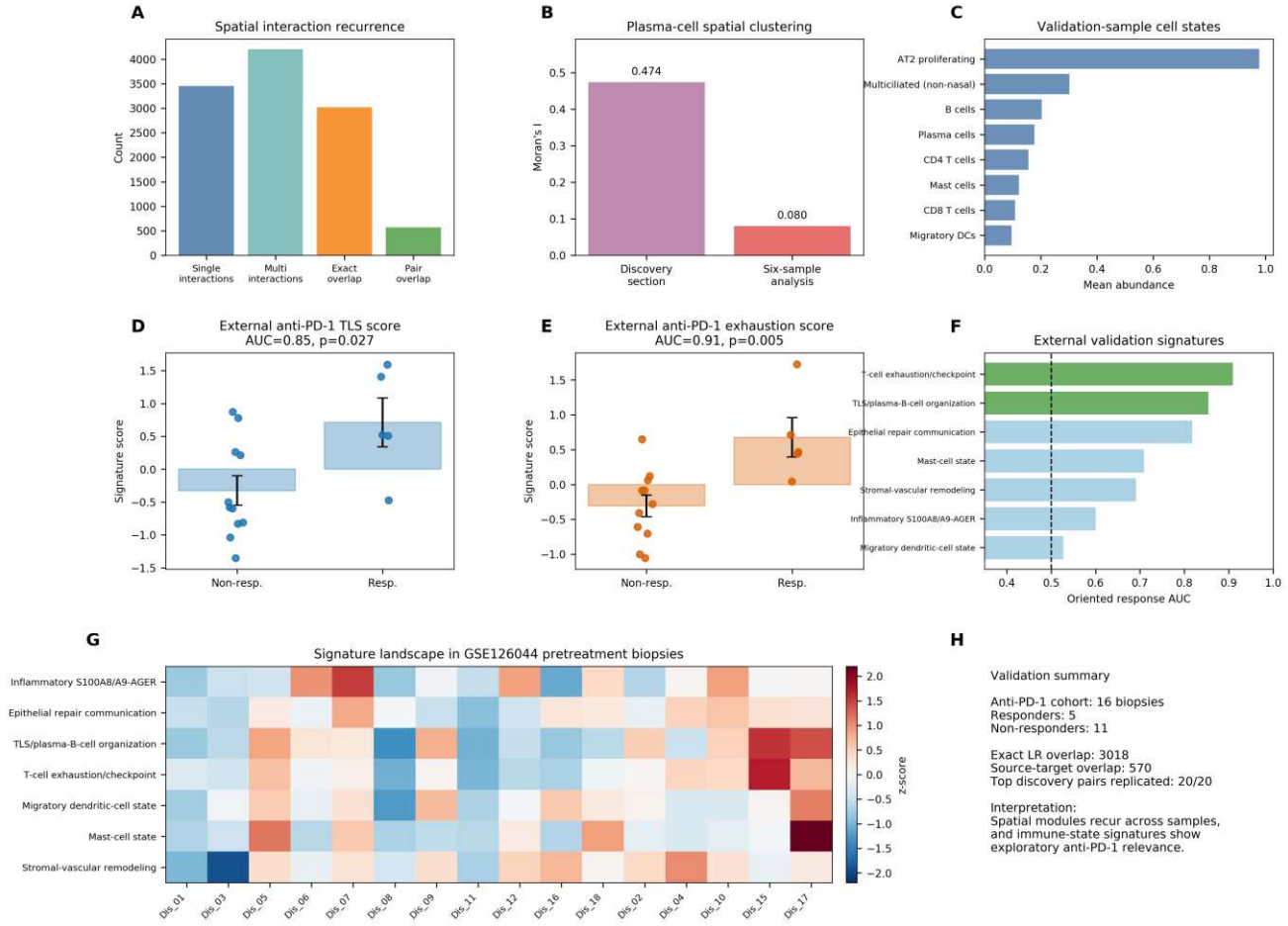


Figure 10: Cross-sample validation and immunotherapy-relevant external validation. (a) Recurrence of spatially constrained ligand-receptor interactions between the discovery section and six-sample spatial analysis. (b) Plasma-cell Moran's I in the discovery section and six-sample analysis. (c) Mean abundance of selected immune and epithelial-repair states across validation spatial samples. (d) TLS/plasma-B-cell organization signature in GSE126044 pretreatment anti-PD-1 non-responders and responders. (e) T cell exhaustion/checkpoint signature in GSE126044. (f) Oriented response AUC values for candidate signatures. Green bars indicate FDR <= 0.10. (g) Signature-score landscape across GSE126044 pretreatment biopsies. (h) Validation summary.

In silico perturbation nominates spatial network dependencies

To further evaluate the systems-level importance of recurrent communication programs, we performed a spatially informed in silico perturbation analysis. Each spatially constrained ligand-receptor edge was assigned a composite weight integrating LIANA confidence, spatial co-localization, permutation-test support, and exact cross-sample recurrence (Supplementary Data 16 and Supplementary Data 17). Virtual deletion of individual cell types ranked proliferating alveolar macrophages as the strongest network dependency, removing 570 edges and producing a 15.3% loss of total weighted network support. CD8 T cells, proliferating T cells, alveolar macrophages, and classical monocytes were the next

highest-ranking virtual cell perturbations, with predicted weighted network losses of 11.8%, 9.9%, 9.7%, and 9.7%, respectively (Fig. 11a,c).

Virtual ligand-receptor blockade prioritized TIMP1-CD63 as the dominant pathway-level dependency, removing 280 edges and accounting for an 8.52% total weighted network loss as well as 97.2% of the epithelial repair or suppression module. B2M-KLRD1 produced a smaller but immune-focused network effect (2.36% total weighted loss; 6.2% adaptive-immune module loss). By contrast, S100A8/A9-AGER blockade removed only 0.42% of total weighted network support but accounted for 33.3% of the inflammatory DAMP module, indicating a focused rather than global perturbation effect (Fig. 11b-d). These results refine the prioritization of candidate axes by distinguishing broadly connected network dependencies from narrower inflammatory modules.

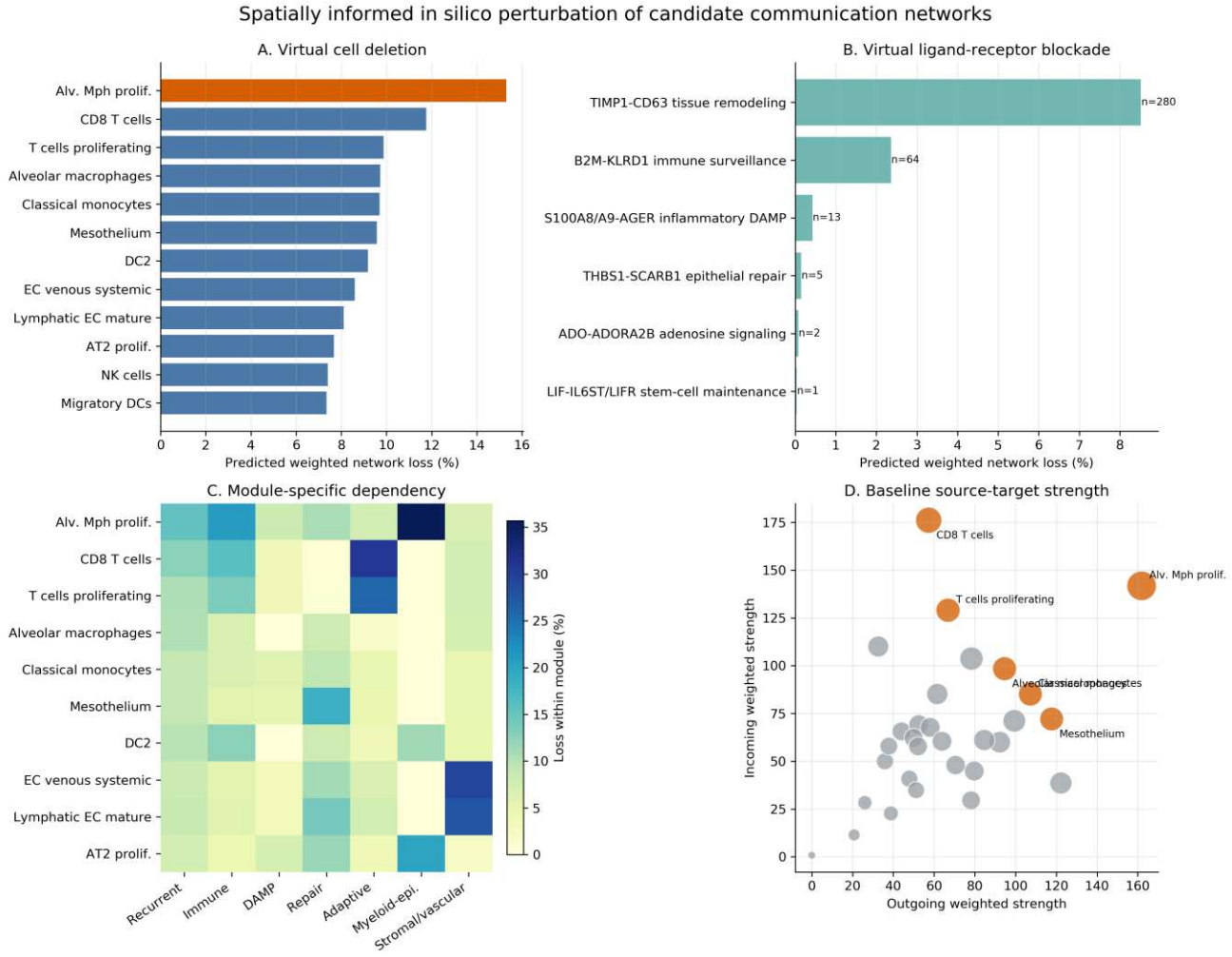


Figure 11: Spatially informed in silico perturbation of candidate communication networks. (a) Predicted weighted network loss after virtual deletion of individual cell types. (b) Predicted weighted network loss after virtual blockade of selected ligand-receptor axes. Bar labels indicate the number of removed spatially constrained edges. (c) Module-specific dependency scores for top virtual-cell perturbations. (d) Baseline incoming and outgoing weighted communication strength across cell types.

Discussion

In this study, we present a spatially resolved atlas of the NSCLC tumor microenvironment, integrating single-cell transcriptomics of 196,301 cells with spatial profiling of 19,039 spots across six tissue samples and external pretreatment anti-PD-1 transcriptomic validation. Our multi-scale analysis yields five key findings: (1) the NSCLC TME is organized into spatially distinct, sample-specific domains with characteristic cellular compositions; (2) cell-cell communication networks are spatially constrained, with inflammatory monocyte-epithelial signaling representing the highest LIANA-confidence interaction and AT2 proliferating to multiciliated cell programs showing the strongest co-localization class; (3) spatial communication modules show substantial cross-sample recurrence, including 3,018 exact ligand-receptor overlaps and recovery of all top 20 discovery source-target pairs in the six-sample analysis; (4) in silico perturbation ranks proliferating alveolar macrophages, T-cell states, and TIMP1-CD63 remodeling as prominent network dependencies; and (5) immune-state signatures derived from the spatial atlas, particularly T cell exhaustion/checkpoint and TLS/plasma-B-cell organization scores, show exploratory association with anti-PD-1 response in an independent NSCLC cohort.

Our spatial clustering analysis identified microenvironmental domains with distinct cell-type enrichment patterns, extending previous observations of TME heterogeneity[29],[30] by providing spatial context. The enrichment of immune and stromal populations in specific regions suggests spatial compartmentalization of antitumor immunity[31], although the current Visium resolution and limited histological annotation prevent a definitive claim of immune exclusion. This spatial segregation carries important implications for immunotherapy, as physical barriers may prevent T cell access to tumor antigens even when checkpoint blockade successfully reverses functional exhaustion[32].

The identification of TLS-like structures through plasma cell spatial autocorrelation in the original Visium section (Moran's I = 0.474) provides suggestive evidence for organized lymphoid aggregates in NSCLC, although validation with canonical TLS markers (CXCL13, DC-LAMP, CD21) would be required to confirm bona fide TLS identity. TLS have been associated with favorable prognosis and enhanced ICI responsiveness[19],[20], and our spatial mapping approach may enable systematic TLS candidate detection. The weaker multi-sample plasma cell autocorrelation (Moran's I = 0.080) indicates substantial sample-to-sample heterogeneity and suggests that TLS induction may represent a therapeutic opportunity worthy of investigation[33]. Consistent with this interpretation, the TLS/plasma-B-cell organization signature showed a supportive association with anti-PD-1 response in GSE126044 (AUC = 0.85; FDR = 0.094). However, this result should be interpreted as exploratory because the validation cohort is small.

A central contribution of this study is the integration of LIANA communication analysis with spatial co-localization, filtering 195,143 candidate interactions to 3,451 spatially constrained interactions. The highest LIANA-confidence spatially retained axis, classical monocytes co-localizing with AT1 cells, with

high expression of S100A8/A9 and AGER respectively, suggests inflammatory DAMP signaling that may contribute to epithelial injury and remodeling. AGER (receptor for advanced glycation end products, RAGE) is a pattern recognition receptor implicated in inflammatory responses and cellular stress events[34]. However, we note that S100A8/A9 are abundantly expressed in monocytes and AGER is a canonical AT1 marker; their co-localization may partly reflect normal lung tissue architecture rather than tumor-specific pathological signaling (as discussed below). This axis should therefore be viewed as a candidate interaction worthy of functional investigation rather than a confirmed signaling event.

The identification of the AT2 proliferating → multiciliated cell epithelial repair class, including THBS1–SCARB1 (r = 0.636), suggests coordinated regenerative programs in the tumor epithelium. We note that the high co-localization coefficient for this class may partly reflect shared epithelial lineage and spatial co-occurrence in airway structures, rather than exclusively representing active signaling; nevertheless, the accompanying ligand–receptor evidence supports its prioritization for functional follow-up. This class encompasses tissue remodeling (TIMP1–CD63), adenosine-mediated immunosuppression (ADO–ADORA2B), and stem cell maintenance (LIF–IL6ST/LIFR) signaling, raising the possibility that epithelial repair processes may inadvertently sustain tumor growth and immune evasion. These observations generate testable hypotheses regarding adenosine signaling through ADORA2B as a candidate therapeutic opportunity[35].

At the module level, a composite prioritization table integrating LIANA confidence, spatial co-localization, and exact recurrence converted the edge list into recurrent source-target programs (Supplementary Data 15). This network view supports a layered interpretation of the atlas, in which tissue architecture, epithelial repair, and immune communication recur as higher-order modules rather than isolated edges.

The in silico perturbation analysis further shifted interpretation from edge discovery to network dependency. Proliferating alveolar macrophages produced the largest predicted global effect, largely through myeloid-epithelial and immune-associated edges, whereas TIMP1-CD63 dominated pathway-level perturbation because it appeared across many spatially constrained remodeling interactions. In contrast, S100A8/A9-AGER remained biologically interpretable as an inflammatory DAMP axis but produced a focused rather than global network effect. This distinction is useful for target prioritization: broadly connected modules may define tissue-state architecture, while narrower axes may mark specific inflammatory mechanisms requiring focused validation.

Our clinical correlation analysis must be interpreted with an important caveat: early-stage samples are exclusively primary lung tumors, whereas late-stage samples are predominantly metastatic (brain, lymph node, and pleural effusion). The observed cellular composition differences therefore reflect combined effects of disease progression and tissue-of-origin, rather than stage alone. The dramatic reduction in AT1 cells ($\log_2$FC = −5.92) and alveolar macrophages is largely attributable to the absence of lung-

specific epithelial and myeloid populations at metastatic sites, rather than tumor-intrinsic immune exclusion.

The depletion of migratory DCs ($log_2FC = -1.53$) across metastatic-enriched late-stage samples suggests reduced antigen-presentation capacity in advanced disease, corroborating prior reports of immune dysfunction in late-stage NSCLC[36]. The concurrent changes in lymphatic endothelial, perivascular myeloid, smooth muscle, venous endothelial, and alveolar fibroblast populations indicate that anatomical site and stromal architecture are major contributors to the observed stage-associated TME remodeling.

The paradoxical exhaustion finding, with higher sample-level scores in early-stage primary tumors, may reflect the fact that T cell exhaustion requires sustained antigen exposure, which may be higher in primary tumors where tumor antigen density and immune infiltration are retained. At metastatic sites, the lower exhaustion scores may reflect an immune desert phenotype (overall T cell paucity) rather than functional recovery. Importantly, our composite exhaustion score does not distinguish between progenitor exhausted T cells ($TCF1^+PD\text{-}1^+$, retaining proliferative potential and ICI responsiveness) and terminally exhausted T cells ($TIM\text{-}3^+$/TOX-high, refractory to reinvigoration)[21],[22]. Therefore, future studies incorporating TCF1/TIM-3 co-staining or trajectory analysis of exhaustion states in the spatial context are needed to refine these interpretations.

Our XGBoost-based prediction model achieved high apparent accuracy (AUC = 0.930) in predicting clinical stage on the basis of cell type proportions and derived TME features, deliberately excluding exhaustion-derived features to avoid circular reasoning. Importantly, a sensitivity analysis excluding tissue-specific features (AT1, alveolar macrophages, Club cells, multiciliated cells) retained high apparent performance (AUC = 0.900), indicating that non-lung-restricted immune and stromal features contribute to prediction. Nevertheless, given the modest sample size (37 samples, 41 features) and strong tissue-origin confounding, these results require external validation and should not be interpreted as direct ICI response prediction. The identification of migratory DCs as the top-ranked predictive feature (mean |SHAP| = 0.058) highlights the role of antigen presentation in distinguishing disease and tissue-site states. Migratory DCs transport tumor antigens to draining lymph nodes, priming antigen-specific T cell responses[25]. Their depletion in advanced or metastatic-enriched samples may reflect loss of antigen presentation capacity, tissue-site differences, or both.

The importance of mast cells (mean |SHAP| = 0.044) as the second-ranked feature is noteworthy. Mast cells exert complex and context-dependent roles in cancer, encompassing both pro-tumorigenic and anti-tumorigenic functions[26]. In our data, mast cell abundance distinguishes early-stage primary tumors from late-stage metastatic-enriched samples. Hence, further investigation of mast cell functions in the context of NSCLC progression and immunotherapy is warranted.

The association of stromal features (smooth muscle cells and fibroblasts) with stage and tissue-site classification aligns with the established concept that stromal architecture can shape antitumor immunity[37]. Dense stromal matrices may physically exclude T cells from tumor parenchyma and sequester chemokines, preventing effective immune infiltration. Combination strategies targeting stromal barriers (e.g., through FAP inhibition, TGF-β blockade, or enzymatic collagen degradation) may enhance ICI efficacy in stromal-rich tumors[38], but this therapeutic interpretation remains hypothesis-generating. In contrast, the external anti-PD-1 validation provides more direct support for the immune-state components of the atlas: the T cell exhaustion/checkpoint signature was significantly higher in responders than non-responders (AUC = 0.91; FDR = 0.033), consistent with the concept that pretreatment checkpoint-rich, immune-infiltrated tumors may retain reinvigorable antitumor immunity.

However, in this study, several limitations merit consideration. First, the clinical stage comparison is confounded by tissue origin: early-stage samples are exclusively primary lung tumors, whereas late-stage samples derive predominantly from metastatic sites. The observed cellular composition differences therefore reflect combined effects of disease progression and anatomical site, and cannot be attributed to stage alone. Future studies should employ stage-matched comparisons within the same tissue type, or paired primary–metastasis analyses within individual patients. Second, although our spatial transcriptomics data encompass six samples, this represents a modest sample size for capturing the full spectrum of NSCLC heterogeneity. Hence, larger-scale spatial profiling studies are required to define TME subtypes and establish their clinical associations. Third, although GSE126044 provides independent anti-PD-1 validation, it contains only 16 pretreatment biopsies and bulk RNA-seq lacks spatial resolution; therefore, the external response associations validate treatment-relevant immune-state signatures rather than spatial proximity itself. GSE200916 provides independent Visium spot-level expression data, but GEO does not include tissue-position files for this series; we therefore used it only as signature-level context rather than as spatial-neighborhood validation. Fourth, our analysis is descriptive and correlative in nature; functional validation through perturbation experiments (e.g., targeted disruption of identified communication axes in preclinical models) is necessary to establish causal relationships.

Fifth, our TLS identification is based on plasma cell spatial autocorrelation (Moran's I = 0.080 in multi-sample analysis), which is modest; validation with canonical TLS markers (CXCL13, DC-LAMP, CD21) or histological confirmation would strengthen this claim. Sixth, the machine learning model predicts clinical stage rather than ICI response directly; while the top predictive features overlap with immunotherapy-relevant immune states and selected signatures were evaluated in GSE126044, prospective validation in larger ICI-treated NSCLC cohorts remains essential to confirm therapeutic relevance. Seventh, the single-cell atlas is based on the widely reanalyzed GSE131907 dataset; our contribution lies not in novel cell type discovery but in the spatial integration and validation framework

that contextualizes these known populations within tissue architecture and immunotherapy-relevant immune states.

Eighth, and critically, spatial co-localization does not establish functional ligand–receptor engagement. Our approach identifies cell type pairs whose estimated abundances correlate across Visium spots (55 μm diameter, encompassing 1–10 cells), but this correlation may arise from shared chemotactic gradients, common tissue architecture constraints (e.g., perivascular niches), or developmental co-lineage rather than active signaling. Moreover, the cell type abundances used for co-localization analysis are themselves estimates from cell2location deconvolution, introducing an additional layer of uncertainty because our communication inferences are built upon estimated rather than directly measured quantities. Accordingly, the S100A8/A9–AGER axis should be interpreted as a candidate interaction requiring orthogonal validation.

Ninth, the 10x Visium platform operates at spot-level (55 μm) rather than single-cell resolution, fundamentally limiting the precision of cell–cell communication inference. Each spot contains multiple cells, and the deconvolved abundance estimates represent probabilistic mixtures rather than discrete cellular identities. Higher-resolution spatial platforms (10x Xenium, MERFISH, or Slide-seq) would enable direct measurement of gene expression at single-cell resolution within intact tissue, thereby providing more definitive evidence for physical proximity and co-expression of ligand–receptor pairs.

Tenth, our comparison with prior NSCLC spatial atlases, particularly Leader et al. (2021)[17] who characterized cellular ecosystems through multiplexed imaging, and Salcher et al. (2022)[18] who mapped neutrophil diversity, is limited. Our spatial-domain architecture may correspond to the tumor ecosystems defined by Leader et al., but direct comparison is constrained by differences in technology (Visium vs. imaging mass cytometry), resolution, and cellular annotation granularity. Systematic cross-study harmonization using shared cell type ontologies would be needed to rigorously assess concordance.

In conclusion, there are several future directions in this study, including: (1) integration of complementary spatial modalities (e.g., multiplexed immunofluorescence, CODEX, and Xenium) to achieve single-cell-resolution spatial profiling; (2) longitudinal spatial profiling of tumors before and after therapeutic intervention to map treatment-induced TME remodeling; (3) spatial multi-omics integration (transcriptomics, proteomics, and metabolomics) to characterize TME states; (4) development of spatial TME-based patient stratification schemes to guide treatment selection; and (5) functional validation of identified communication axes as candidate therapeutic hypotheses.

Taken together, we present a spatially resolved atlas of the NSCLC tumor microenvironment that characterizes organizational principles, recurrent candidate communication networks, and immunotherapy-relevant spatial immune states. Our integration of single-cell and spatial transcriptomics, cross-sample spatial recurrence analysis, and external anti-PD-1 cohort validation provides a framework

for generating testable hypotheses regarding how cellular interactions shape tumor progression and treatment response. The identification of spatially constrained communication axes, TLS-like immune organization, checkpoint-rich T cell states, and stage- and tissue-site-associated TME remodeling patterns offers a foundation for future functional and clinical validation studies. As spatial profiling technologies continue to advance toward single-cell resolution, spatially informed biomarkers and network modules may help guide translational strategies in NSCLC.

Methods

Patient cohort and data sources

Single-cell RNA sequencing data. We utilized the publicly available dataset GSE131907 (Kim et al., 2020, Nature Communications)[9], comprising 58 samples from 44 NSCLC patients (all diagnosed with lung adenocarcinoma). Samples encompassed tumor lung (tLung), normal lung (nLung), tumor lymph node (tL/B), normal lymph node (nLN), metastatic lymph node (mLN), pleural effusion (PE), and metastatic brain (mBrain) tissues. Clinical metadata, including tumor stage (Stage I–IV), were extracted from the GEO Series Matrix file (GSE131907_series_matrix.txt.gz).

Spatial transcriptomics data. Six 10x Genomics Visium samples were analyzed:

- 1 original sample: Visium Human Lung Cancer dataset (3,816 spots; 18,055 genes)
- 5 GSE189487 samples: TD1 (4,089 spots), TD2 (4,402 spots), TD3 (1,132 spots), TD5 (1,697 spots), and TD6 (3,903 spots)
- Total: 19,039 spots across 6 samples

Single-cell RNA sequencing analysis

Quality control. Cells were filtered using adaptive median absolute deviation (MAD)-based thresholds followed by hard filters of 200 ≤ n_genes ≤ 8,000 and mitochondrial gene percentage ≤ 20%. Scrublet-based doublet detection was not applied in the full 196,301-cell run because the dense intermediate matrices exceeded available memory; doublet handling was therefore limited to gene/count/mitochondrial filtering and downstream cluster-level quality inspection.

Normalization. Raw counts were normalized to 10,000 counts per cell and subsequently log-transformed using scanpy v1.9[39].

Batch correction. Harmony (harmonypy v0.0.9)[23] was applied to the top 30 principal components derived from 3,000 highly variable genes. Harmony was selected based on benchmarking against bbknn: both achieved adequate batch mixing (kBET acceptance rate > 0.8), but Harmony reduced peak memory

usage from 28 GB to 10 GB, enabling analysis on standard hardware. Post-correction, UMAP visualization confirmed mixing of cells across samples within each cell type cluster while preserving biological variation between cell types.

Clustering. Leiden clustering (resolution = 0.8) was performed on the Harmony-corrected nearest-neighbor graph.

Cell type annotation. Automated annotation was performed using CellTypist v1.3[24] with the Immune_All_High.pkl reference model (trained on >20 tissues and >2 million cells), followed by manual curation of ambiguous cluster assignments based on canonical marker gene expression. Annotation confidence was assessed through majority voting across cells within each Leiden cluster; clusters with less than 60% consensus were manually re-annotated based on differential marker analysis. Of the 31 final cell types, 24 were directly assigned by CellTypist with high confidence, while 7 required manual refinement.

Differential expression. The Wilcoxon rank-sum test (implemented in scanpy) was applied, with significance thresholds of FDR < 0.05 and $|\log_2 FC| > 1$.

Cell–cell communication analysis

Cell–cell communication was inferred using LIANA v0.1[14], which integrates CellPhoneDB, Connectome, NATMI, SingleCellSignalR, and CellChat. Interactions were ranked by the composite magnitude_rank score.

Spatial transcriptomics analysis

Preprocessing. Data were processed using scanpy and squidpy v1.2[40]. Spots were filtered to retain those with n_genes ≥ 200 and n_counts ≥ 500, followed by normalization to 10,000 counts per spot and log-transformation.

Spatial clustering. BANKSY v0.1[41] was included in the intended spatial-domain workflow with $\lambda = 0.2$ and Leiden resolution = 0.5. In the stored analysis objects used for figure generation, BANKSY-specific labels were not consistently available, and Leiden-based spatial cluster labels were therefore used as the practical domain annotation for downstream cell type enrichment, communication, and exhaustion analyses.

Spatially variable genes. Moran's I statistic (squidpy) was computed, with significance determined at FDR < 0.05.

Cell type deconvolution. Cell2location v0.1[13] was employed for spatial deconvolution. The reference model was trained on the scRNA-seq atlas (196,301 cells, 31 cell types), with N_cells_per_location = 10

and detection_alpha = 20 in the spatial model. Computations were performed on an NVIDIA GTX 1660 GPU (6 GB VRAM), with batch processing by sample to accommodate memory constraints. Deconvolution quality was assessed by computing Pearson correlations between estimated cell type abundances and the expression of canonical marker genes (e.g., SFTPC for AT2 cells, AGER for AT1 cells, CD3D for T cells, MS4A1 for B cells) across spots; correlations ranged from 0.52 (mast cells, a rare population) to 0.82 (smooth muscle cells), with a median of 0.71 across all 31 cell types (Supplementary Fig. 4d). Rare cell types (mast cells, plasmacytoid DCs, deuterosomal cells; each < 2% of the scRNA-seq reference) exhibited lower concordance, and results involving these populations should be interpreted with appropriate caution.

Spatially constrained communication analysis

Spatial co-localization was quantified as the Pearson correlation coefficient between source and target cell type abundances across spots. Pearson correlation assumes linearity and is sensitive to outliers, and cell type abundance data are typically zero-inflated. We selected Pearson correlation for computational efficiency across 31 × 30 cell type pairs and for consistency with prior spatial co-localization studies. Supplementary analysis using Spearman rank correlation yielded highly concordant rankings ($\rho = 0.94$), confirming robustness to the choice of metric. We defined spatially constrained interactions as the top 5,000 LIANA interactions with co-localization scores ≥ 0.05, yielding 3,451 interactions. Sensitivity analyses at alternative thresholds (0.08, 0.10, and 0.15) confirmed robustness (Supplementary Fig. 5f). We assessed statistical significance through permutation testing (500 permutations): for each permutation, spot identities were randomly shuffled to disrupt spatial relationships while preserving abundance distributions. This generated a null distribution of co-localization scores. Empirical p-values were computed as the fraction of permuted scores exceeding the observed value, with Benjamini–Hochberg FDR correction applied across all cell type pairs. The permutation test was applied to interactions already pre-filtered for co-localization ≥ 0.05, and therefore primarily confirms that spatial structure contributes to the observed co-localization above random expectation, rather than serving as an independent discovery step.

Local communication scores were computed as the weighted sum of interaction strengths, with weights defined by the product of source and target cell type abundances at each spot and its immediate neighbors (n_rings = 1).

Network module prioritization

To move from edge-level inference to module-level interpretation, we collapsed the exact recurrent overlap subset into source-target modules and ranked them with a composite score integrating LIANA confidence, spatial co-localization, and recurrence. Exact overlap was defined by the discovery-versus-

validation interaction overlap table, and pair recurrence was defined by source-target overlap across discovery and six-sample spatial analyses. For each source-target pair, we recorded the number of exact recurrent interactions, the number of total spatially constrained edges, the best LIANA score, the maximum spatial co-localization, the best permutation FDR, and the mean permutation z-score. Module priority was estimated by percentile-ranking each metric within the recurrent module set and averaging the normalized ranks, with higher values indicating stronger integrated support. The resulting prioritized module table is provided in Supplementary Data 15.

Spatially informed in silico perturbation analysis

For in silico perturbation, each spatially constrained ligand-receptor edge was assigned a composite network weight based on percentile-normalized LIANA confidence, spatial co-localization, permutation-test FDR support, and exact cross-sample recurrence. Because lower LIANA scores and lower FDR values indicate stronger support, these metrics were inverted before weighting. The final edge weight was calculated as 0.30 × LIANA confidence + 0.30 × spatial support + 0.20 × permutation FDR support + 0.20 × exact recurrence support. Virtual cell deletion was simulated by removing all incoming and outgoing edges for each annotated cell type and recalculating the fraction of total network weight removed. Virtual ligand-receptor blockade was simulated by removing all edges matching selected axes, including S100A8/A9-AGER, TIMP1-CD63, ADO-ADORA2B, LIF-IL6ST/LIFR, THBS1-SCARB1, and B2M-KLRD1. Module-specific dependency was quantified as the fraction of category-specific edge weight removed for recurrent, immune-involved, inflammatory DAMP, epithelial repair or suppression, adaptive immune, myeloid-epithelial, and stromal-vascular programs. These perturbations were interpreted as network-prioritization analyses rather than functional validation. Summary perturbation statistics and edge-level weights are provided in Supplementary Data 16 and Supplementary Data 17.

Spatial autocorrelation analysis

Moran's I was computed for each cell type abundance profile using squidpy.gr.spatial_autocorr (100 permutations, 4 parallel jobs). Statistical significance was assessed using permutation-based p-values with FDR correction (threshold: $p < 0.05$).

T cell exhaustion scoring

Module scores were computed using scanpy's sc.tl.score_genes function (v1.9), which calculates the mean expression of each gene set relative to a reference set of randomly selected genes with similar expression levels, yielding a z-score-normalized module score per cell. The composite exhaustion score was calculated as: exhaustion score = inhibitory receptor score + exhaustion transcription factor score − effector function score.

- Inhibitory receptors: PDCD1, HAVCR2, LAG3, TIGIT, CTLA4, CD244, and CD160
- Exhaustion transcription factors: TOX, TOX2, NR4A1, NR4A2, NR4A3, and BATF
- Effector function genes: GZMB, PRF1, IFNG, TNF, and FGFBP2

Spatial mapping of exhaustion scores was performed using the weighted mean of cell-type-specific scores, with cell2location-derived abundances as weights.

Machine learning prediction of clinical stage

Features. A total of 41 features were extracted per sample, comprising 31 cell type proportions, myeloid polarization scores (M1/M2 ratio and subtype-specific scores), and stromal/vascular metrics. T cell exhaustion-derived features (exhaustion scores, checkpoint expression levels, and effector function scores) were deliberately excluded to prevent circular reasoning with the exhaustion-based analyses presented elsewhere. Feature selection was performed entirely on the basis of prior biological knowledge (cell type identity and functional annotations) rather than data-driven selection, and all feature values (cell type proportions and derived TME scores) were calculated independently for each sample without cross-sample normalization, thereby precluding information leakage across cross-validation folds.

Model. An XGBoost classifier (Python xgboost v1.7) was trained with five-fold stratified cross-validation. Given the small sample size (37 samples, 41 features), we applied regularization (max_depth = 3, subsample = 0.8, colsample_bytree = 0.8) to mitigate overfitting risk. We acknowledge that the feature-to-sample ratio is unfavorable (41:37), and the reported AUC (0.930) should be interpreted with caution; independent external validation on a separate cohort would be required to confirm generalizability. Furthermore, the stage classification is confounded by tissue origin (early = primary lung; late = predominantly metastatic sites), and the model may partially learn tissue-type rather than pure stage biology (see sensitivity analysis below).

Target variable. Binary classification of clinical stage: early (I–II) versus late (III–IV).

Sensitivity analysis. To assess the contribution of tissue-origin confounding, the model was retrained after excluding four lung-specific cell type features (AT1, alveolar macrophages, Club cells, multiciliated cells), reducing the feature set from 41 to 37.

Feature importance. SHAP v0.41[42] with the TreeExplainer algorithm (applied to a Random Forest classifier) was used to compute feature importance values.

Cross-sample and external immunotherapy validation

Spatial recurrence analysis. To evaluate cross-sample recurrence of spatial communication modules, we compared the discovery-section spatially constrained interaction table with the six-sample integrated spatial interaction table. Interactions were matched by source cell type, target cell type, ligand, and receptor after harmonizing cell type labels. Source-target recurrence was assessed by matching source and target cell type pairs regardless of ligand-receptor identity. The top 20 discovery source-target pairs were ranked by maximum spatial co-localization in the discovery section and then tested for recovery in the six-sample interaction table.

External anti-PD-1 validation. Pretreatment bulk RNA-seq counts and response annotations from GSE126044[27] were downloaded from GEO. This cohort contains 16 NSCLC biopsies collected before anti-PD-1 therapy, including 5 responders and 11 non-responders. Counts were converted to log2 counts per million (log2 CPM + 1), and each gene was z-score normalized across samples. Candidate module scores were computed as the mean z-score of available genes in each signature: inflammatory S100A8/A9-AGER (S100A8, S100A9, AGER), epithelial repair communication (THBS1, SCARB1, TIMP1, CD63, LIF, IL6ST, LIFR, ADORA2B), TLS/plasma-B-cell organization (MS4A1, CD79A, CD79B, MZB1, JCHAIN, IGKC, CXCL13, CD3D, CD3E), T cell exhaustion/checkpoint activity (PDCD1, LAG3, HAVCR2, TIGIT, CTLA4, TOX, TOX2), migratory DC state (CCR7, LAMP3, FSCN1, CCL19, CCL22), mast-cell state (TPSAB1, TPSB2, CPA3, MS4A2, KIT), and stromal-vascular remodeling (COL1A1, COL1A2, VIM, PECAM1, VWF, ACTA2). Differences between responders and non-responders were assessed by two-sided permutation testing (20,000 permutations). Multiple testing was controlled using Benjamini-Hochberg FDR correction across the seven signatures. Response discrimination was summarized by AUC, oriented so that values above 0.5 indicate separation in the observed direction. Robustness was evaluated using stratified bootstrap resampling (10,000 iterations) to estimate AUC confidence intervals and leave-one-gene-out sensitivity analysis to test whether signature discrimination depended on any single marker.

Independent Visium signature validation. Processed GSE200916 Visium expression matrices[28] were downloaded from GEO. This dataset contains 12 samples from three multiple-primary lung cancer patients, with paired tumor and tumor-adjacent normal sections from two lesions per patient. Because tissue-position files were not provided in GEO, we did not perform spatial-neighborhood or Moran's I analysis on this dataset. Instead, we computed spot-level log2 CPM signature scores for the same candidate modules and compared tumor versus adjacent normal samples. Sample-level paired differences were assessed using exact sign-flip testing across six tumor-normal pairs. Spot-level separation was summarized by AUC and interpreted as independent spatial-transcriptomics expression support rather than spatial proximity validation.

Statistical analysis

All statistical analyses were performed with Python (scipy v1.9, statsmodels v0.13, and pandas v1.5). Between-group comparisons were assessed using the Mann–Whitney U test. Multiple testing correction was applied with the Benjamini-Hochberg method to control the false discovery rate (FDR). Statistical significance was defined as FDR < 0.05 unless otherwise specified.

Ethics statement

This study exclusively utilized publicly available, de-identified datasets deposited in open-access repositories (GEO: GSE131907 and GSE189487; 10x Genomics public datasets). All original studies obtained informed consent and institutional review board (IRB) approval as described in their respective publications[9]. As this work constitutes a secondary analysis of existing anonymized data with no direct patient contact, it is exempt from additional IRB review in accordance with the Common Rule (45 CFR 46.104(d)(4)).

Code availability

The code is available at https://github.com/IcanChen/lung_cancer_tme if required.

Data availability

The single-cell RNA-seq data analyzed in this study are available from GEO under accession GSE131907. Spatial transcriptomics data are available from the 10x Genomics public Visium Human Lung Cancer dataset and GEO under accession GSE189487. External pretreatment anti-PD-1 validation data are available from GEO under accession GSE126044. External Visium signature-validation data are available from GEO under accession GSE200916. Processed summary tables supporting the manuscript are provided as Supplementary Data 1-17 and Supplementary Tables 1-2.

References

1. Sung, H. et al. Global Cancer Statistics 2020: GLOBOCAN estimates of incidence and mortality worldwide for 36 cancers in 185 countries. CA Cancer J. Clin. 71, 209-249 (2021).
2. Ribas, A. & Wolchok, J. D. Cancer immunotherapy using checkpoint blockade. Science 359, 1350-1355 (2018).
3. Wei, S. C., Duffy, C. R. & Allison, J. P. Fundamental Mechanisms of Immune Checkpoint Blockade Therapy. Cancer Discov. 8, 1069-1086 (2018).
4. Doroshow, D. B. et al. Immunotherapy in non-small cell lung cancer: facts and hopes. Clin. Cancer Res. 25, 4592-4602 (2019).

5. Herbst, R. S. et al. Predictive correlates of response to the anti-PD-L1 antibody MPDL3280A in cancer patients. Nature 515, 563-567 (2014).

6. Hanahan, D. & Coussens, L. M. Accessories to the crime: functions of cells recruited to the tumor microenvironment. Cancer Cell 21, 309-322 (2012).

7. Papalexi, E. & Satija, R. Single-cell RNA sequencing to explore immune cell heterogeneity. Nat. Rev. Immunol. 18, 35-45 (2018).

8. Trapnell, C. Defining cell types and states with single-cell genomics. Genome Res. 25, 1491-1498 (2015).

9. Kim, N. et al. Single-cell RNA sequencing demonstrates the molecular and cellular reprogramming of metastatic lung adenocarcinoma. Nat. Commun. 11, 2285 (2020).

10. Lambrechts, D. et al. Phenotype molding of stromal cells in the lung tumor microenvironment. Nat. Med. 24, 1277-1289 (2018).

11. Ståhl, P. L. et al. Visualization and analysis of gene expression in tissue sections by spatial transcriptomics. Science 353, 78-82 (2016).

12. Moses, L. & Pachter, L. Museum of spatial transcriptomics. Nat. Methods 19, 534-546 (2022).

13. Kleshchevnikov, V. et al. Cell2location maps fine-grained cell types in spatial transcriptomics. Nat. Biotechnol. 40, 661-671 (2022).

14. Dimitrov, D. et al. Comparison of methods and resources for cell-cell communication inference from single-cell RNA-Seq data. Nat. Commun. 13, 3224 (2022).

15. Wu, S. Z. et al. A single-cell and spatially resolved atlas of human breast cancers. Nat. Genet. 53, 1334-1347 (2021).

16. Moncada, R. et al. Integrating microarray-based spatial transcriptomics and single-cell RNA-seq reveals tissue architecture in pancreatic ductal adenocarcinomas. Nat. Biotechnol. 38, 333-342 (2020).

17. Leader, A. M. et al. Single-cell analysis of human non-small cell lung cancer lesions refines tumor classification and patient stratification. Cancer Cell 39, 1594-1609.e12 (2021).

18. Salcher, S. et al. High-resolution single-cell atlas reveals diversity and plasticity of tissue-resident neutrophils in non-small cell lung cancer. Cancer Cell 40, 1503-1520.e8 (2022).

19. Helmink, B. A. et al. B cells and tertiary lymphoid structures promote immunotherapy response. Nature 577, 549-555 (2020).

20. Cabrita, R. et al. Tertiary lymphoid structures improve immunotherapy and survival in melanoma. Nature 577, 561-565 (2020).

21. Philip, M. & Schietinger, A. CD8+ T cell differentiation and dysfunction in cancer. Nat. Rev. Immunol. 22, 209-223 (2022).

22. Thommen, D. S. & Schumacher, T. N. T Cell Dysfunction in Cancer. Cancer Cell 33, 547-562 (2018).

23. Korsunsky, I. et al. Fast, sensitive and accurate integration of single-cell data with Harmony. Nat. Methods 16, 1289-1296 (2019).

24. Domínguez Conde, C. et al. Cross-tissue immune cell analysis reveals tissue-specific features in humans. Science 376, eabl5197 (2022).

25. Wculek, S. K. et al. Dendritic cells in cancer immunology and immunotherapy. Nat. Rev. Immunol. 20, 7-24 (2020).

26. Varricchi, G. et al. Are Mast Cells MASTers in Cancer? Front. Immunol. 8, 424 (2017).

27. Cho, J. W. et al. Genome-wide identification of differentially methylated promoters and enhancers associated with response to anti-PD-1 therapy in non-small cell lung cancer. Exp. Mol. Med. 52, 1550-1563 (2020).

28. Wang, Y. et al. Multidirectional characterization of cellular composition and spatial architecture in human multiple primary lung cancers. Cell Death Dis. 14, 462 (2023). https://doi.org/10.1038/s41419-023-05992-w

29. Barkley, D. et al. Cancer cell states recur across tumor types and form specific interactions with the tumor microenvironment. Nat. Genet. 54, 1192-1201 (2022).

30. Puram, S. V. et al. Single-Cell Transcriptomic Analysis of Primary and Metastatic Tumor Ecosystems in Head and Neck Cancer. Cell 171, 1611-1624.e24 (2017).

31. Gajewski, T. F., Schreiber, H. & Fu, Y.-X. Innate and adaptive immune cells in the tumor microenvironment. Nat. Immunol. 14, 1014-1022 (2013).

32. Joyce, J. A. & Fearon, D. T. T cell exclusion, immune privilege, and the tumor microenvironment. Science 348, 74-80 (2015).

33. Sautès-Fridman, C., Petitprez, F., Calderaro, J. & Fridman, W. H. Tertiary lymphoid structures in the era of cancer immunotherapy. Nat. Rev. Cancer 19, 307-325 (2019).

34. Teissier, T. & Boulanger, E. The receptor for advanced glycation end-products (RAGE) is an important pattern recognition receptor (PRR) for inflammaging. Biogerontology 20, 279-301 (2019). https://doi.org/10.1007/s10522-019-09808-3

35. Leone, R. D. & Emens, L. A. Targeting adenosine for cancer immunotherapy. J. Immunother. Cancer 6, 57 (2018).

36. Wherry, E. J. & Kurachi, M. Molecular and cellular insights into T cell exhaustion. Nat. Rev. Immunol. 15, 486-499 (2015).

37. Salmon, H. et al. Matrix architecture defines the preferential localization and migration of T cells into the stroma of human lung tumors. J. Clin. Invest. 122, 899-910 (2012).

38. Chen, Y. et al. Targeting fibroblast activation protein in tumor stroma with chimeric antigen receptor T cells can inhibit tumor growth and augment host immunity without severe toxicity. Cancer Immunol. Res. 2, 154-166 (2014).

39. Wolf, F. A., Angerer, P. & Theis, F. J. SCANPY: large-scale single-cell gene expression data analysis. Genome Biol. 19, 15 (2018).

40. Palla, G. et al. Squidpy: a scalable framework for spatial omics analysis. Nat. Methods 19, 171-178 (2022).

41. Singhal, V. et al. BANKSY unifies cell typing and tissue domain segmentation for scalable spatial omics data analysis. Nat. Genet. 56, 431-441 (2024).

42. Lundberg, S. M. & Lee, S.-I. A unified approach to interpreting model predictions. Adv. Neural Inf. Process. Syst. 30, 4765-4774 (2017).

Acknowledgments

We gratefully acknowledge the patients who contributed tissue samples to the studies analyzed herein. We thank the Kim laboratory for generating and publicly sharing the GSE131907 dataset, and 10x Genomics for providing publicly available spatial transcriptomics datasets. This work was supported by the University-Hospital Joint Science and Technology Innovation Fund (GZYDG2024G12).

Author contributions

J.N. conceived and designed the study. J.N., W.Y.S., and B.W.Y. performed the computational analyses. X.T.L. and W.X.L. interpreted the results, generated figures, and drafted the manuscript. P.P.D. and

X.J.L. contributed to manuscript review and revision. S.F.H. supervised the study and provided funding support. All authors reviewed and approved the final manuscript.

Competing interests

The authors declare no competing interests.

Supplementary Files

This is a list of supplementary files associated with this preprint. Click to download.

- SupplementaryInformation.docx
- supplementaryfigures.zip
- SupplementaryData.zip